

A Numerical Study of Gravity Wave Breaking and Impacts on Turbulence and Mean State

H.-L. LIU* AND P. B. HAYS

Space Physics Research Laboratory, Department of Atmospheric, Oceanic and Space Sciences, University of Michigan, Ann Arbor, Michigan

R. G. ROBLE

High Altitude Observatory, National Center for Atmospheric Research,⁺ Boulder, Colorado

(Manuscript received 30 December 1997, in final form 18 September 1998)

ABSTRACT

A model system is established that includes three interactive components: a dynamics model, a turbulence model, and a chemistry model. The dynamics model solves the two-dimensional, nonlinear, nonhydrostatic, compressible, and viscous flow equations, and the turbulence model is adapted from the 2.5-level Mellor–Yamada turbulence model with minor adjustments. The dynamics and the turbulence models are coupled with a chemistry model to study the mesoscale impacts of gravity wave breaking on the atmospheric compositional structures. The present study focuses on the local distribution of atomic oxygen and ozone. The model system is used to study the gravity wave propagation, growth, breakdown, and its impacts on the mean state in the middle and upper atmosphere. The inclusion of a turbulence model makes it possible to study the long-term evolution of the gravity wave after wave breaking and in the presence of nonuniform turbulence, as well as the interaction between a breaking wave and turbulence. The turbulence model parameterizes the three-dimensional mixing due to the flow instability and it eliminates the unrealistically strong supersaturation observed in previous two-dimensional simulations. The modeling result suggests that the induced acceleration due to convective instability may lead to strong shear, which causes dynamical instability at lower altitudes. The result reveals the interdependence of waves and turbulence and shows that the turbulence energy density due to instability has similar temporal and spatial characteristics to previous radar observations. The result is also compared with the linear saturation theory, and it is found that the eddy diffusion coefficients in the wave-breaking region are nonuniform, and the average values are less than those obtained from the linear saturation theory. The result also suggests that the inclusion of the turbulence model could be a valid approach to study the averaged two-dimensional gravity wave and turbulence features after wave breaking. More adjustments of the turbulence model parameters, according to upper-atmosphere observations and turbulence physics studies using large eddy simulation and direct numerical simulation methods for three-dimensional gravity wave–breaking processes, are necessary to improve the model performance in future studies.

1. Introduction

Atmospheric internal gravity waves can affect both mesoscale and planetary-scale dynamics in the mesosphere and thermosphere regions. In these regions, nonlinear interactions between gravity waves generated at lower altitudes become more important and the waves may become unstable. Due to the nonlinear wave in-

teractions and instability, the waves may saturate and a certain amount of the wave momentum is deposited into the mean flow, which causes mean flow acceleration or deceleration. In this process, turbulence can be generated, which in turn helps restore the wave stability.

Gravity wave saturation was first analyzed by Hodges (1969) and further studied in a more general context by Lindzen (1981). It was assumed in both works that convective instability leads to wave breakdown, and above the breaking level the eddy diffusion is strong enough to offset any further growth of wave amplitude. Based on this assumption, the analytical form of horizontal and vertical velocity perturbations above the breaking level was obtained and the vertical momentum flux and the mean flow acceleration were derived, which shows that the acceleration is in the direction of the wave intrinsic phase velocity and approximately proportional to

* Current affiliation: HAO/NCAR, Boulder, Colorado.

⁺ The National Center for Atmospheric Research is sponsored by the National Science Foundation.

Corresponding author address: Han-Li Liu, HAO/NCAR, P.O. Box 3000, Boulder, CO 80307-3000.
E-mail: liuh@ucar.edu

the third power of the intrinsic phase speed. Lindzen's formulation was applied to the parameterization of wave drag in general circulation models by Holton (1982, 1983) and Miyahara (1984), and it was shown to be an improvement over the Rayleigh drag formulation.

This parameterization is based on the linear gravity wave theory; therefore, nonlinear effects, which could be significant before and after wave breaking, were not considered. Nonlinear wave interaction may cause diffusion and gravity wave saturation (Weinstock 1976, 1982). Diffusivity in both horizontal and vertical directions thus derived shows anisotropic features similar to observations. On the other hand, works by Lindzen and Forbes (1983), Fritts (1985), and Dunkerton (1987) showed that nonlinear wave interactions cannot lead to wave saturation, though the upward momentum can be reduced. This parameterization assumes a uniform turbulence in the breaking region, so it cannot represent the turbulence dependence on the local wave structures. The implication of this assumption, especially on the turbulence Prandtl number, has been discussed by Chao and Schoeberl (1984), Fritts and Dunkerton (1985), and Coy and Fritts (1988).

Numerical studies have been conducted to study the process of gravity wave breaking and the transition to turbulence. Klaassen and Peltier (1985a) studied the detailed breaking process of two-dimensional finite amplitude Kelvin–Helmholtz waves and found that there exists energy exchange between the wave and the mean flow. Though small-scale fluctuations are produced during this process, the onset of turbulence is not observed and the large-scale coherent structure persists. This is presumably due to the lack of the third dimension. In Klaassen and Peltier (1985b), it was shown that the two-dimensional Kelvin–Helmholtz waves are unstable with respect to three-dimensional perturbations and these perturbations can lead to longitudinally symmetric secondary instabilities. A two-dimensional model more specific for the middle atmosphere studies was developed by Walterscheid and Schubert (1990), which is a nonlinear, nonhydrostatic, and compressible model to study the evolution, breakdown, and saturation of a two-dimensional internal gravity wave. The model was able to resolve the mean flow acceleration due to wave transience and initial wave breaking. It also indicated that large and localized turbulence can result from the unstable stratification, and suggested that the parameterization by a linear saturation theory tends to be an overestimate. However, the turbulence model employed in the study was not sufficient to resolve the turbulence mixing after the wave becomes unstable. This causes the persisting strong overturning of potential temperature, which was shown to be unrealistic by later three-dimensional simulations (Andreassen et al. 1994; Fritts et al. 1994; Isler et al. 1994). These authors developed a numerical model that solves the three-dimensional nonlinear and compressible Euler equations using a spectral collocation method. The high resolution of the

spectral method enables the study of the fine structures of wave breaking. The numerical results show that the initial wave overturning leads to a secondary instability that consists of pairs of counterrotating vortex structures stretching in the direction perpendicular to the wave phase line, which cannot be properly represented in the two-dimensional modeling. This makes the supersaturation in the three-dimensional case persist much shorter than in the two-dimensional case. The three-dimensional vortex structures also enhance the vertical mixing of momentum; therefore, the acceleration is smaller above the unstable region and larger below compared with the three-dimensional case. These results are consistent with earlier analysis by Klaassen and Peltier (1985a,b). The three-dimensional direct numerical simulation, on the other hand, might be limited to the moderate Reynolds number range.

The purpose of this investigation is to build a self-consistent and efficient model system that can simulate the simultaneous interactions between gravity waves, the mean state, and turbulence. For this purpose, a dynamics model was developed to solve the two-dimensional nonlinear, nonhydrostatic, and compressible Navier–Stokes equations, incorporating the 2.5-level Mellor–Yamada turbulence model (Mellor and Yamada 1982) for its closure. The turbulence model is slightly adjusted and modified for this application. The dynamics model is used to simulate gravity wave propagation and growth in the middle and upper atmosphere considering a background wind and a realistic background temperature. It is also used to study the long-term evolution of the nonuniform turbulence structures and the interaction between gravity waves and turbulence after wave breaking for relatively large Reynolds numbers. The model can resolve the wave–mean flow interaction due to wave transience, wave breaking, and turbulent diffusion, and it facilitates the study of gravity wave spectra and their relation with wave breaking, Doppler shift, and nonlinear interaction. The latter topic will be discussed in a separate paper. It should be pointed out that the turbulence model adapted for the current application was originally developed for problems in the troposphere and the atmospheric boundary layer (Mellor and Yamada 1982), and it has been extensively tested and used for stratified geophysical flows with shear and/or convective instability. However, the turbulence processes during gravity wave breaking may not be the same, and future research needs to be done to understand the differences and to adjust the model according to turbulence physics studies (e.g., Kaltenbach et al. 1994; Fritts et al. 1998).

2. Numerical model

There are three interactive components in the model system: 1) a solver for the two-dimensional, nonlinear, nonhydrostatic, compressible, and viscous flow equations; 2) the 2.5-level Mellor–Yamada turbulence clo-

sure model; and (3) a mesosphere–thermosphere–ionosphere chemistry model, which is a longitude slice of the National Center for Atmospheric Research (NCAR) thermosphere–ionosphere–mesosphere–electrodynamics general circulation model (TIME GCM) (Roble 1995; Roble and Ridley 1994; Roble et al. 1987) with slight modifications.

a. Dynamics model

The two-dimensional dynamics equations used in this study are

$$\frac{\partial \rho}{\partial t} + \nabla \cdot (\rho \mathbf{v}) = 0 \quad (1)$$

$$\frac{\partial \mathbf{v}}{\partial t} + \mathbf{v} \cdot \nabla \mathbf{v} + \frac{1}{\rho} \nabla p + g \mathbf{k} = \mathbf{D}_M \quad (2)$$

$$\frac{\partial \theta}{\partial t} + \mathbf{v} \cdot \nabla \theta = D_H + \frac{Q}{c_p \rho T} \quad (3)$$

$$p = \rho R \theta \left(\frac{p}{p_s} \right)^\kappa, \quad (4)$$

where

$$\mathbf{D}_M = \nu \frac{\partial^2 \mathbf{v}}{\partial x^2} + \frac{\partial}{\partial z} \left((\nu + K_M) \frac{\partial}{\partial z} \mathbf{v} \right)$$

$$D_H = \nu \frac{\partial^2 \theta}{\partial x^2} + \frac{\partial}{\partial z} \left((\nu + K_H) \frac{\partial \theta}{\partial z} \right) - \frac{\partial}{\partial z} \left((\nu + K_{H0}) \frac{\partial \theta_0}{\partial z} \right)$$

$$\mathbf{v} = (u, w)$$

$$\nabla = \left(\frac{\partial}{\partial x}, \frac{\partial}{\partial z} \right)$$

$$\mathbf{k} = (0, 1)$$

$$\kappa = R/c_p,$$

and ρ , \mathbf{v} , and θ are atmosphere mass density, velocity vector, and potential temperature, respectively. The molecular viscosity coefficient is assumed to be equal to the molecular diffusion coefficient and is denoted as ν in the equations. The eddy diffusion coefficients are K_M and K_H and are calculated by the turbulence model, which will be discussed below. In the energy equation [(3)] Q is the heating rate, which incorporates dynamical and chemical heating. The subscript 0 denotes initial mean values of the corresponding variables.

This set of equations is derived from the Navier–Stokes equations but the Coriolis force is neglected. Molecular diffusion is calculated in both horizontal and vertical directions, while only vertical eddy diffusion is considered to account for turbulence mixing. The initial background state is in hydrostatic and radiative equilibrium. Due to initial radiative equilibrium, the thermal diffusion related to the initial temperature structure

should be subtracted from the total diffusion so that the initial conductive heat flux is zero.

The fully compressible form of the continuity equation is used because of the convenience in the numerical integration of the equations, as well as a better representation of physical reality. Walterscheid and Schubert (1990) noticed that dynamical effects of compressibility should be considered for fast waves.

In the computation, an equivalent set of equations is used, where potential temperature and Exner pressure are the state variables (Tapp and White 1976). Those perturbation variables that grow exponentially with altitude are normalized by multiplying them by the square root of the the atmosphere density, $\sqrt{\rho_0}$.

A staggered grid system is chosen in the computation for spatial discretization. The staggered grid system implicitly increases computational accuracy and more naturally observes conservation laws. It also enables a more consistent treatment of lower-boundary conditions. Second-order center difference schemes are used in the vertical direction. The horizontal grids are usually coarser than the vertical grids to save computational loads when the horizontal structures are assumed to be relatively simple. The coarseness of these grids is compensated for by using a fourth-order central difference scheme in the horizontal direction. Besides increased accuracy, the central difference schemes are also easy to parallelize when necessary. In the following numerical experiments, the vertical grid size is 1 km while the horizontal grid size is 3 km.

Temporal integration is advanced semi-implicitly. The explicit scheme for the nondiffusion terms is the second-order Adam–Bashforth method, with the second-order Runge–Kutta method for the start-up computation, while the implicit scheme for the vertical diffusion is the Crank–Nicolson method. For the explicit integration, the time step is limited by the fast acoustic wave modes. To increase computing efficiency, a splitting scheme is used to integrate the fast acoustic wave modes and the slower gravity wave modes separately so that the Courant–Friedrichs–Lewy (CFL) condition can be satisfied for all the modes. This approach is similar to that proposed by Klemp and Wilhelmson (1978a,b).

For the problems in this study, periodic boundary condition is used for the lateral boundaries of the domain. At the lower boundary, the flow is assumed to be inviscid and the lower-boundary condition is a specified vertical velocity perturbation, while the other variables are consistently and implicitly specified through the flow equations. During the implicit time steps, the velocity and potential temperature perturbations at the lower boundary are set equal to the values in the explicit time step because of the inviscid assumption. At the upper boundary, an absorbing boundary scheme is implemented, where Rayleigh friction terms are added to the momentum equations and the Rayleigh friction coefficients are gradually increased in the layer to avoid wave

reflection. The initial state of the computation is in hydrostatic and radiative equilibrium. The stratification of the atmosphere can be specified by using different temperature and wind profiles for different cases.

To avoid nonlinear aliasing and false energy cascading, a low-pass implicit spatial filter is applied to equation variables at each time step. The filter scheme is similar to that suggested by Pepper et al. (1979), which completely eliminates Nyquist waves (2-h waves) and applies almost no damping for higher wavenumber components. The filter is applied to the horizontal direction of the model and not the vertical, because the advective nonlinearity in the vertical direction is less severe and the small-scale waves can be strongly damped by the vertical diffusion.

b. Turbulence model

The turbulence model used in this numerical study is the 2.5-level second-moment closure model described in Mellor and Yamada (1982) and Yamada (1983), which has been used extensively in various geophysical applications. Flows with free and forced convection were calculated by the model and compared favorably with observations (Mellor and Yamada 1982). Potential temperature and wind variations in the atmospheric boundary layer were calculated by Yamada and Mellor (1975). The dispersion of scalars can also be studied by the model, and Yamada (1977) calculated the three-dimensional dispersion of a chemically inert pollutant species. The model has also been modified to study two-dimensional or near-two-dimensional problems (Dobosy 1979; Yamada 1983). This turbulence model is summarized below.

The fundamental closure assumptions of this model are the energy redistribution hypothesis of Rotta and the Kolmogorov hypothesis of local small-scale isotropy. The former assumes that the correlation terms between pressure and velocity gradients work against anisotropy and the latter determines the turbulence dissipation rate. The model relates all the second-order turbulence correlation terms, the so-called mean Reynolds stress (MRS) by Mellor and Herring (1973), to the turbulence energy density and turbulence "master" length scale; it is assumed that all the turbulence scales are proportional to a master length scale. The turbulence energy density and the master length scale are prognostically determined from the model,

$$\frac{\partial q^2/2}{\partial t} + \mathbf{v} \cdot \nabla q^2/2 - \frac{\partial}{\partial z} \left(lqS_q \frac{\partial q^2/2}{\partial z} \right) = P_s + P_b - \varepsilon \quad (5)$$

$$\frac{\partial q^2 l}{\partial t} + \mathbf{v} \cdot \nabla q^2 l - \frac{\partial}{\partial z} \left(lqS_q \frac{\partial q^2 l}{\partial z} \right) = lE_l(P_s + P_b) - l\varepsilon, \quad (6)$$

where $q^2/2$ and l are turbulence energy density and master length scale; $S_q = 0.2$ and $E_l = 1.8$ are scale con-

stants; and P_s , P_b , and ε are shear production, buoyant production, and dissipation of the turbulence, respectively, and are calculated by

$$P_s = -\langle w''u'' \rangle \frac{\partial u}{\partial z} = K_M \left(\frac{\partial u}{\partial z} \right)^2 \quad (7)$$

$$P_b = \beta g \langle w''\theta'' \rangle = -gK_H \frac{1}{\theta} \frac{\partial \theta}{\partial z} \quad (8)$$

$$\varepsilon = \frac{q^3}{\Lambda_1} = \frac{q^3}{B_1 l}, \quad (9)$$

where $B_1 = 16.6$ is another scale constant. Double primes are used for the subgrid-scale turbulence perturbations and $\langle \rangle$ for the ensemble average of these subgrid perturbations. In Eqs. (7) and (8) the Reynolds stress term and the turbulence heat flux term are replaced by the mean state gradient terms using the eddy diffusion coefficients K_M and K_H , which are in turn determined by

$$K_M = lqS_M \quad (10)$$

$$K_H = lqS_M/Pr_t. \quad (11)$$

As shown in the dynamics equations, only the vertical eddy diffusion is considered. The turbulence Prandtl number Pr_t is dependent on the Richardson number Ri and varies between 0.76 and 0.89. Here S_M is a scale factor that is also dependent on the Richardson number and quantifies the intensity of eddy mixing at different Richardson number range. It becomes larger as Richardson number decreases. The detailed formulation of these variables can be found in the references mentioned above. It can be seen from Eqs. (5) and (6) that the turbulence is determined by the shear and buoyant production and dissipation, as well as advective and diffusive transport.

Several adjustments of the turbulence model have been made for this study. Because there is no physical boundary near the turbulence region, the distance from a wall is assumed to be infinitely large and an associated term is dropped from the original master length scale equation. We also assume that the spatial grid size is an upper limit for the master length scale. It should be noted that the formulation and the parameters are open to further adjustment because the details of turbulence dynamics may differ from the cases studied by Mellor and Yamada. These adjustments could be made in future studies by comparing the results with the direct numerical simulation–large eddy simulation (DNS–LES) results, and with observation studies if possible.

Similar to solving the dynamics equations, a semi-implicit scheme is used to treat the diffusion and non-diffusion terms separately in solving the 2.5-level model system. At the lower boundary, the flow is assumed to be inviscid and q^2 and $q^2 l$ are set to very small values; at the upper boundary, an open boundary condition is applied to both q^2 and $q^2 l$:

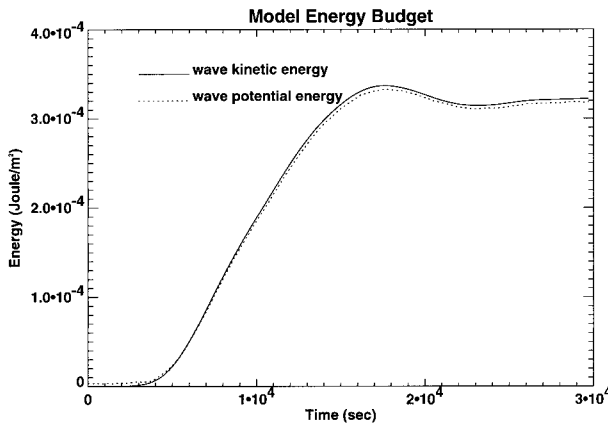


FIG. 1. The column density of wave kinetic and potential energy when the wave amplitude is small and linear assumption is still valid in the effective computation domain. Equal partition between the kinetic and the potential energy is closely observed.

$$\frac{\partial q^2}{\partial z} = 0 \tag{12}$$

$$\frac{\partial q^2 l}{\partial z} = 0. \tag{13}$$

The turbulence model used here is not self-starting; therefore, it is necessary to set a nonzero initial turbulence background. On the other hand, this background turbulence should be small enough so that it will not damp the wave in any significant way.

c. Chemistry model

To study the interactions between the mesosphere and the thermosphere chemistry and dynamics, especially the impacts of breaking gravity waves and turbulence, a chemistry model is incorporated into the dynamics model. The chemistry model is a longitude slice of the TIME GCM (Roble 1995; Roble and Ridley 1994; Roble et al. 1987) with slight modifications. The compositional structures include the density profiles of electrons, ions, and the major and minor neutral gas species, and they are affected by the dynamical transport processes such as turbulence mixing in that region. The calculation is performed in a self-consistent way by coupling the physical and chemical processes in the mesosphere, the thermosphere, and the ionosphere. In this study, the focus is the local effects of wave breaking and turbulence on the distribution of atomic oxygen and ozone in the mesosphere–mesopause region.

3. Analysis of results

Four numerical experiments are presented in the following sections, hereafter labeled as cases 1, 2, 3, and 4. In all of these experiments, the altitude range of the effective computational domain is from 50 to 140 km, and the horizontal dimension is 150 km. The gravity

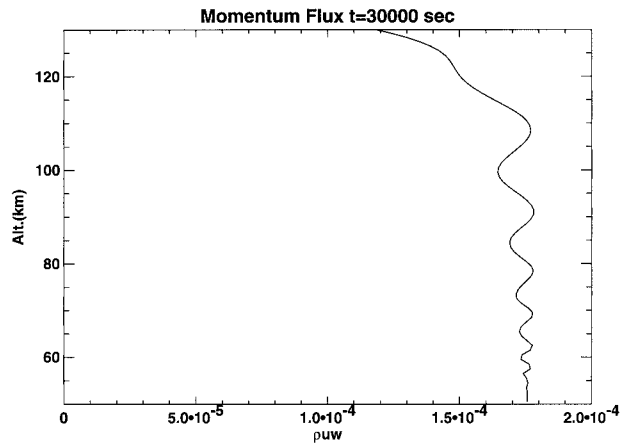


FIG. 2. Average momentum flux (unit: N m⁻²) of the gravity wave at *t* = 30 000 s.

wave sources are specified at the lower boundary with horizontal wavelength of 150 km and wave period of 2500 s. In section 3a the amplitude of the gravity wave source is small enough so that the wave is approximately linear in the whole computational domain (case 1). In section 3b two similar experiments are performed, one (case 2) without a turbulence model and the other (case 3) with one. Case 4, in section 3c, is similar to case 3, except that the perturbation amplitude in case 4 is twice as large as that in case 3. The details of each experiment will be discussed in the corresponding sections.

a. Comparison with linear theory

In case 1, a sinusoidal wave source is imposed at the lower boundary of the computational domain at 50 km by perturbing the vertical velocity. The amplitude of the vertical velocity at that level is increased to its maximum value, $5 \times 10^{-4} \text{ m s}^{-1}$, over one wave period and remains the same afterward. This maximum amplitude is set to a very small value to ensure that the wave perturbation is small enough in the whole computational domain so that linear approximation is valid, making it possible to compare the results with the linear theory. This is used to test the model capability in conserving the total mass, momentum, and energy.

The effective upper boundary is at 140 km and a sponge layer is added above. The background temperature is isothermal with $T_0 = 239 \text{ K}$ at all altitudes, and the background wind is zero. Molecular viscosity and diffusion are considered in the momentum and energy equations. The vertical wavelength is 18 km according to the linear dispersion relation, which gives a vertical phase velocity of -7.2 m s^{-1} (vertical group velocity of 7.2 m s^{-1}). Therefore, it takes about 15 000 s for the gravity wave to fully grow between 50 and 140 km. The total modeling time is set to 30 000 s in the experiment.

The total mass is calculated and the maximum relative

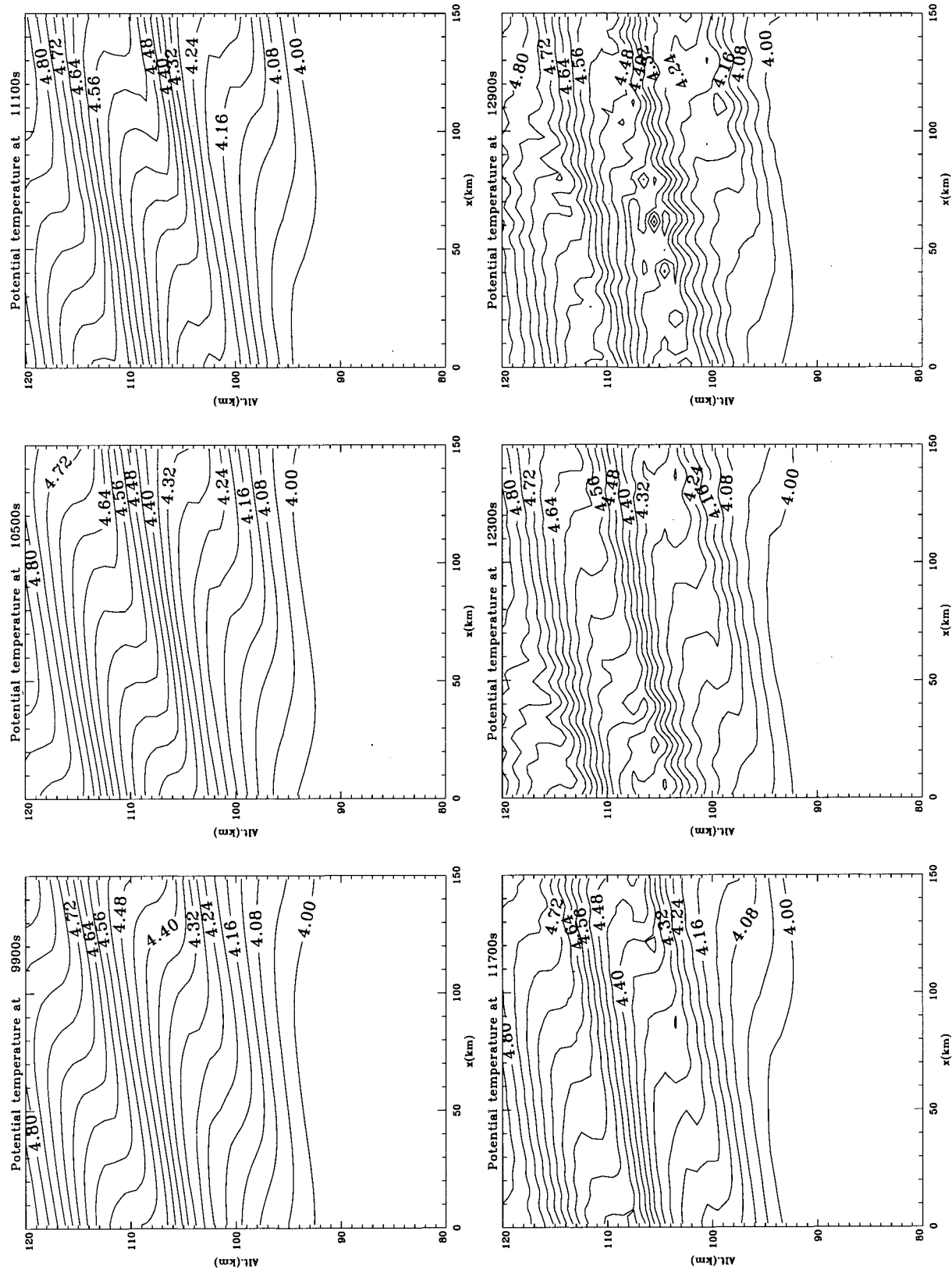


FIG. 3. Potential temperature ($\log_{10}\theta$) field before and after wave breaking for case 2. No turbulence model is used in this case.

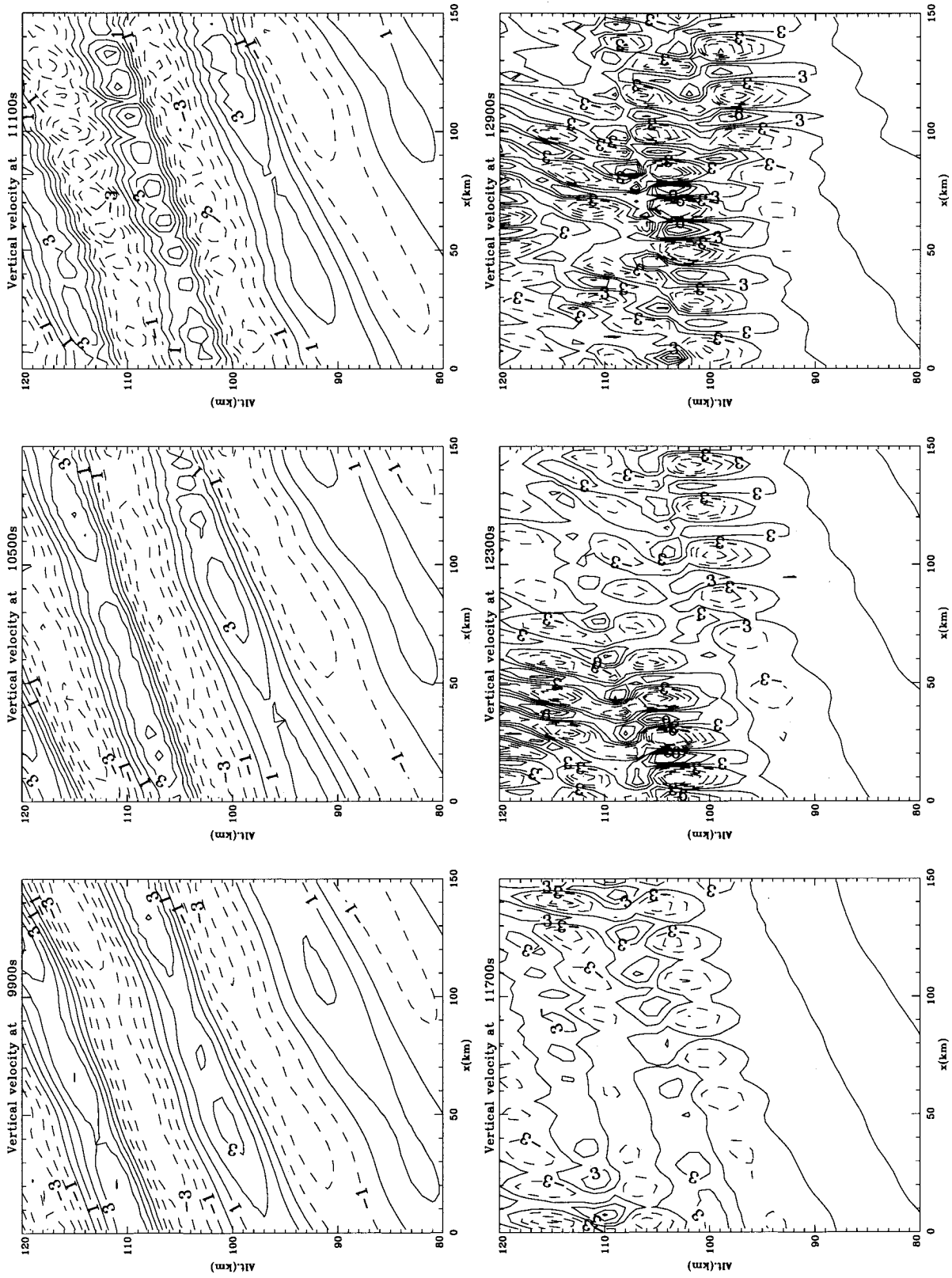


FIG. 4. Vertical velocity field at the same time steps as Fig. 3. Cellular structures develop in the wave-breaking region. The contour range is (upper) from -5 to 5 m s^{-1} with 1 m s^{-1} intervals and (lower) from -15 to 15 m s^{-1} with 3 m s^{-1} intervals. Dashed contour lines are for negative values.

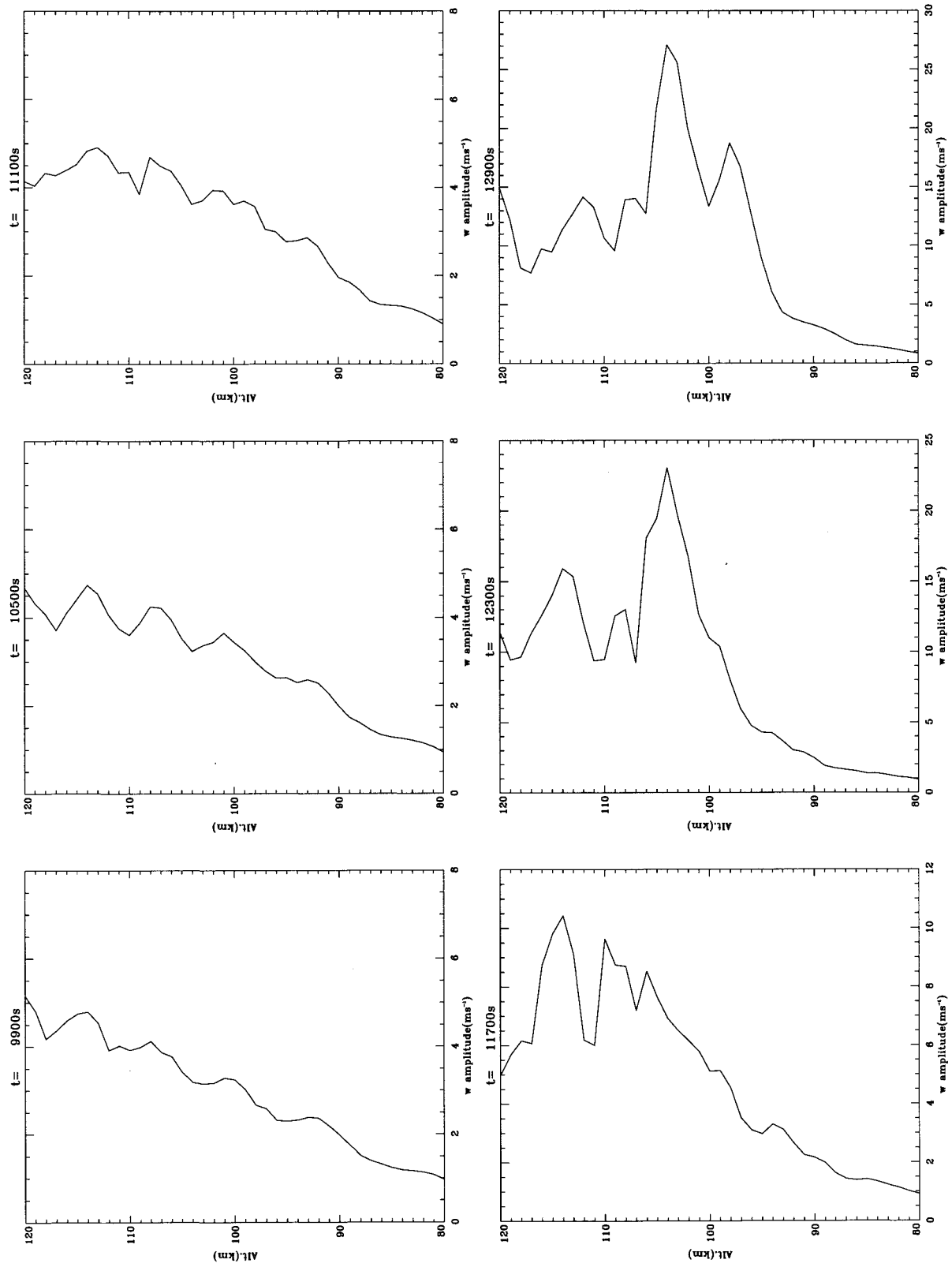


FIG. 5. Vertical profiles of the vertical velocity amplitude in case 2. There is no evidence of wave saturation.

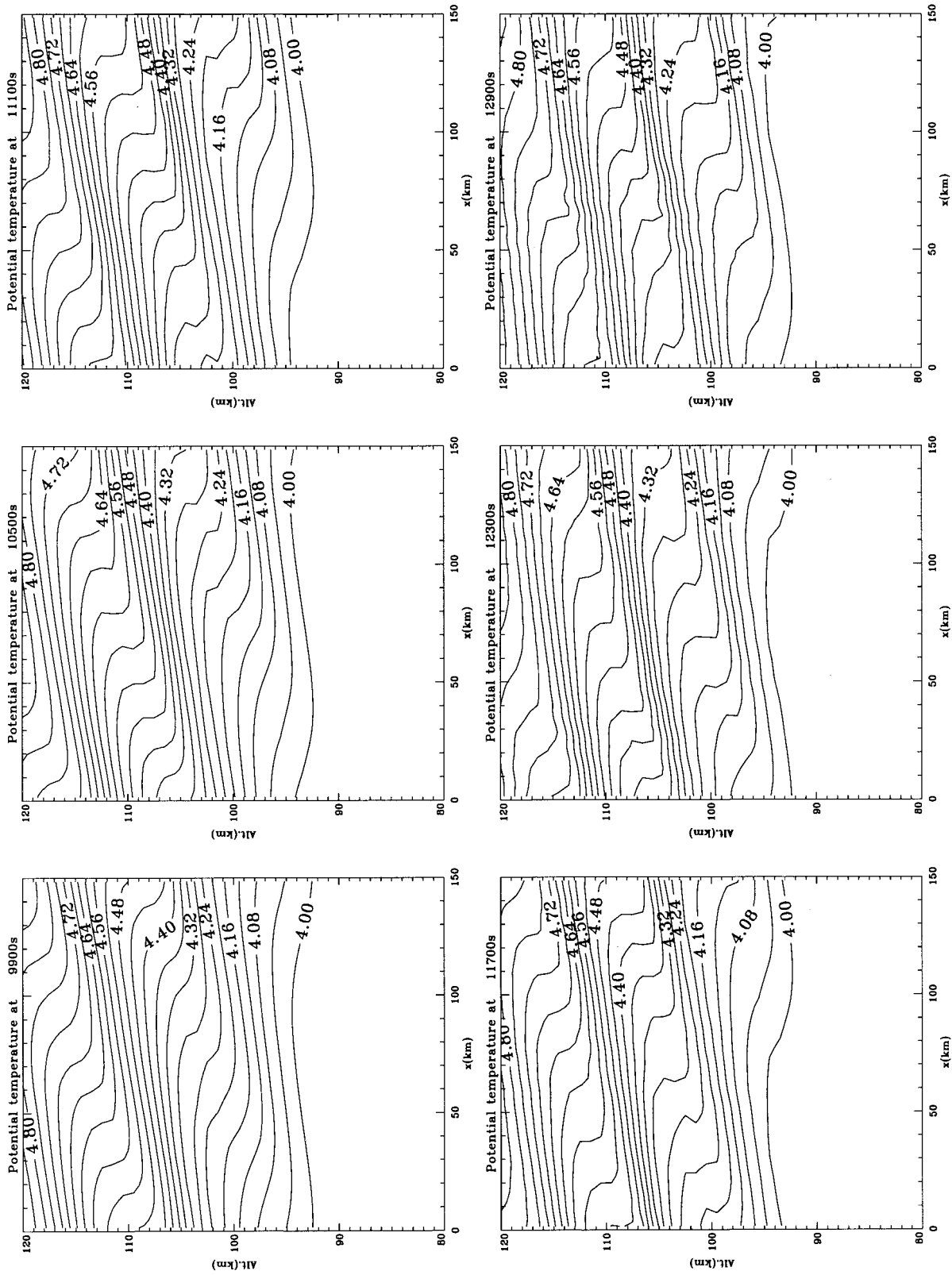


FIG. 6. As in Fig. 3 but for case 3 where the turbulence closure model is used.

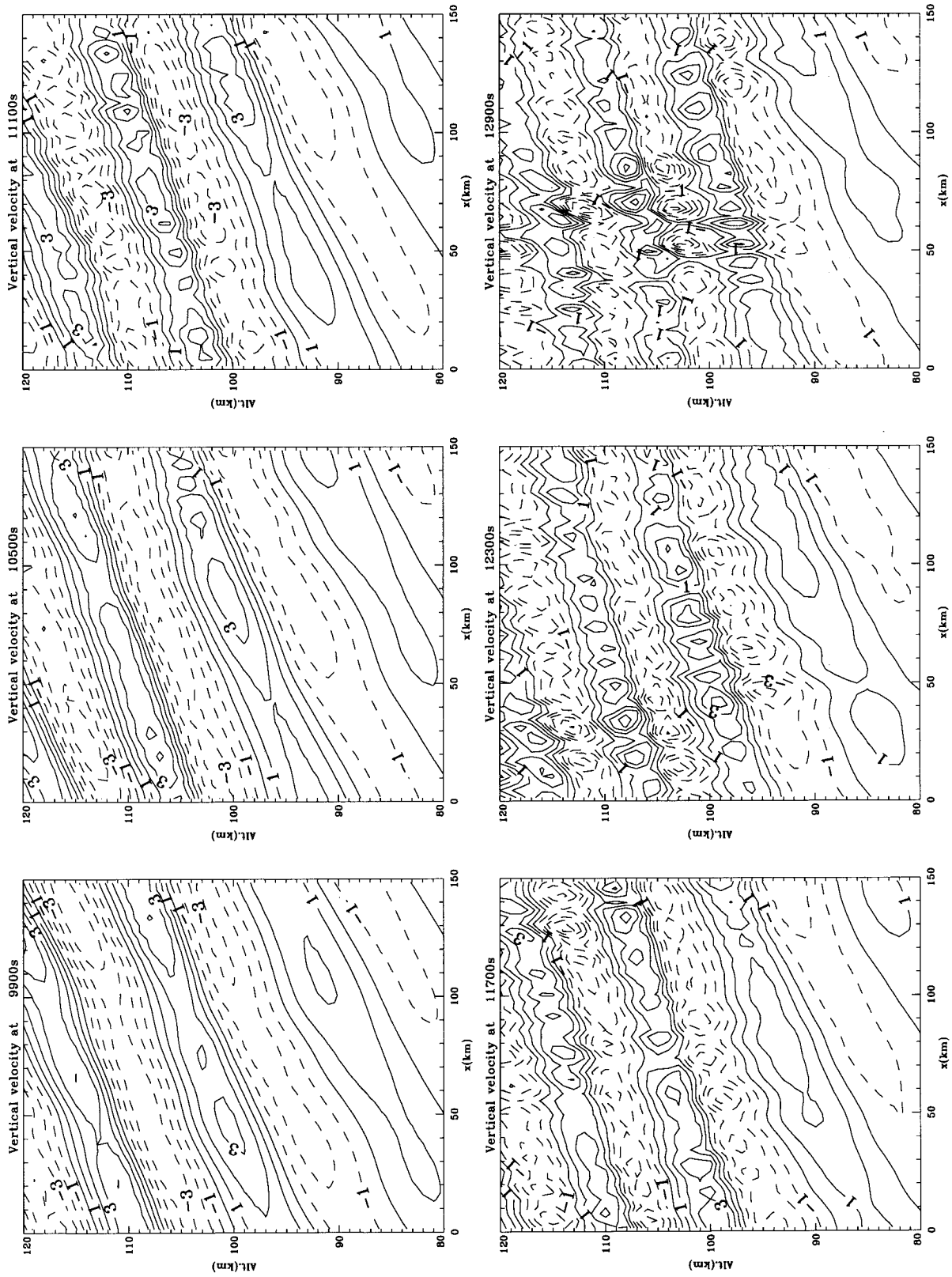


FIG. 7. As in Fig. 4 but for case 3 where the turbulence closure model is used.

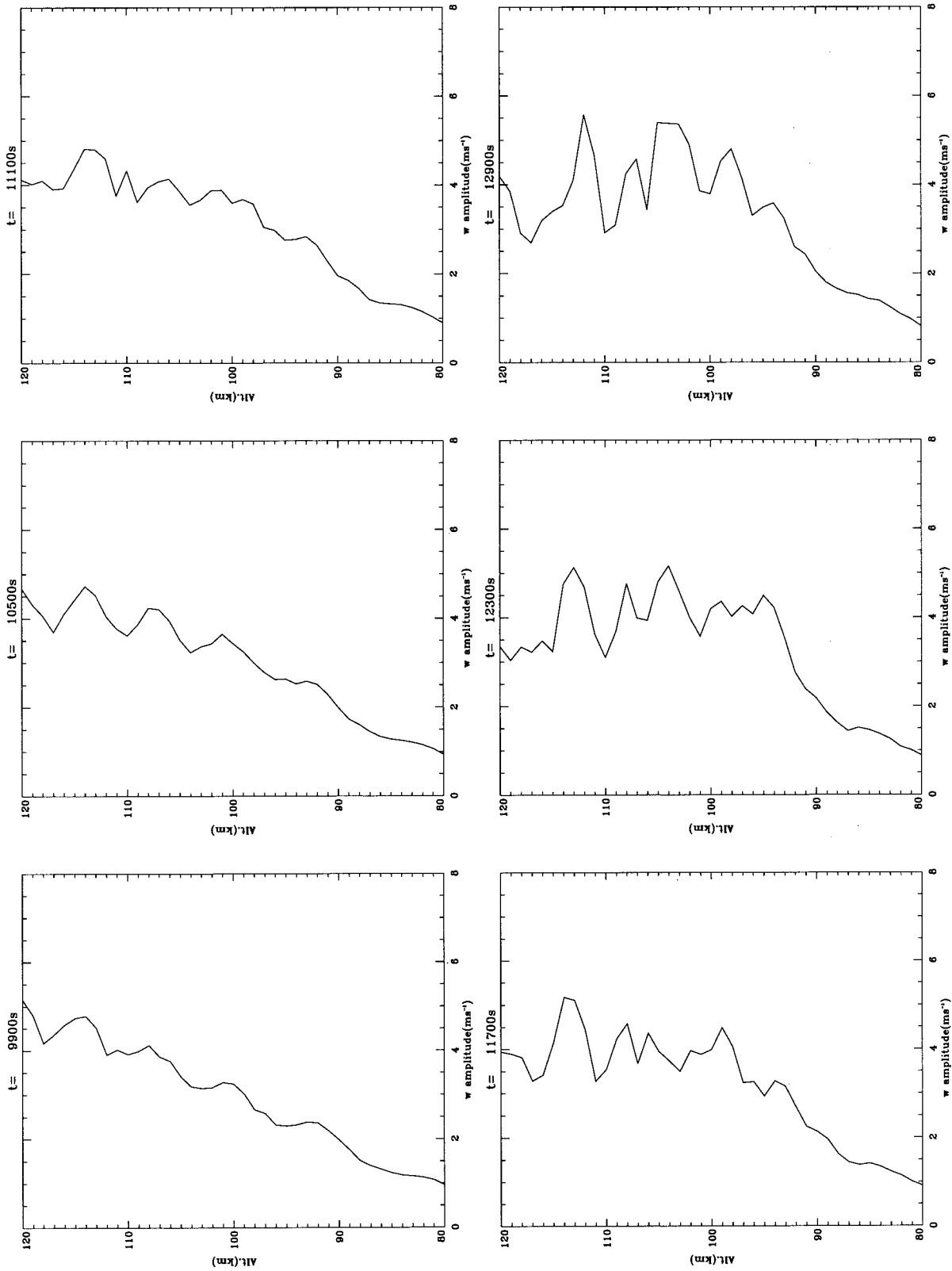


FIG. 8. As in Fig. 5 but for case 3 where the turbulence closure model is used. The wave amplitude saturation can be observed after wave breaking.

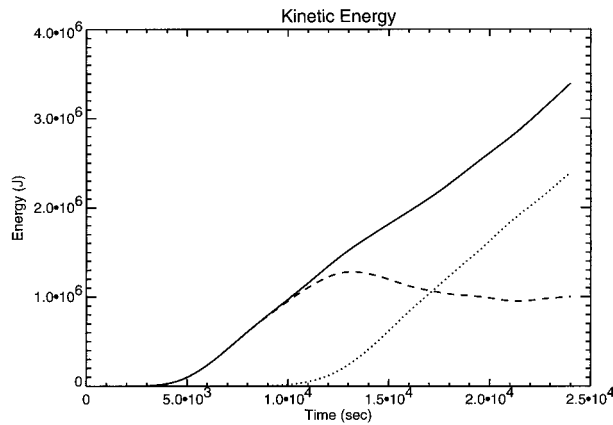


FIG. 9. Total kinetic energy in the effective computational domain of a breaking gravity wave. Solid line, total kinetic energy; dotted line, average kinetic energy; dashed line, wave kinetic energy.

deviation of the total mass with respect to the initial value is less than 1×10^{-5} , or 0.001%, during the simulation. Therefore, the total mass is conserved in the computation.

The column density (total energy divided by the horizontal wavelength and a unit length for the third dimension) of wave kinetic energy and potential energy are shown in Fig. 1. They increase from zero to the maximum in about 17 000 s as the wave grows. In this

process, the two forms of energy are nearly equal, demonstrating the equal partition of the kinetic and potential energy of the wave system. Both decrease slightly after the peak value and then stay at the same level when the wave becomes steady and the energy input at the lower boundary is balanced by the outgoing energy at the upper boundary of the effective computation domain. There is no false accumulation of wave energy in the process.

Figure 2 shows the vertical profile of the momentum flux averaged over one wavelength. The average flux is positive due to the upward propagation of the wave. Below 110 km, the flux is approximately independent of altitude, a manifest of the Eliassen–Palm theorem and an indication that there is no false wave reflection or wave–mean flow interaction. Above 110 km, the momentum flux decreases due to increasing damping effects by molecular viscosity.

This damping effect can also be seen by comparing the horizontal and vertical velocity perturbations calculated from the model and those from the analytic theory. There is no obvious deviation from the linear theory below 105 km, but above 105 km the amplitude of the wave calculated from the model becomes smaller than that of the linear wave. This is most obvious at the maximum amplitude, because it is also the location where the second derivatives of the velocity with respect

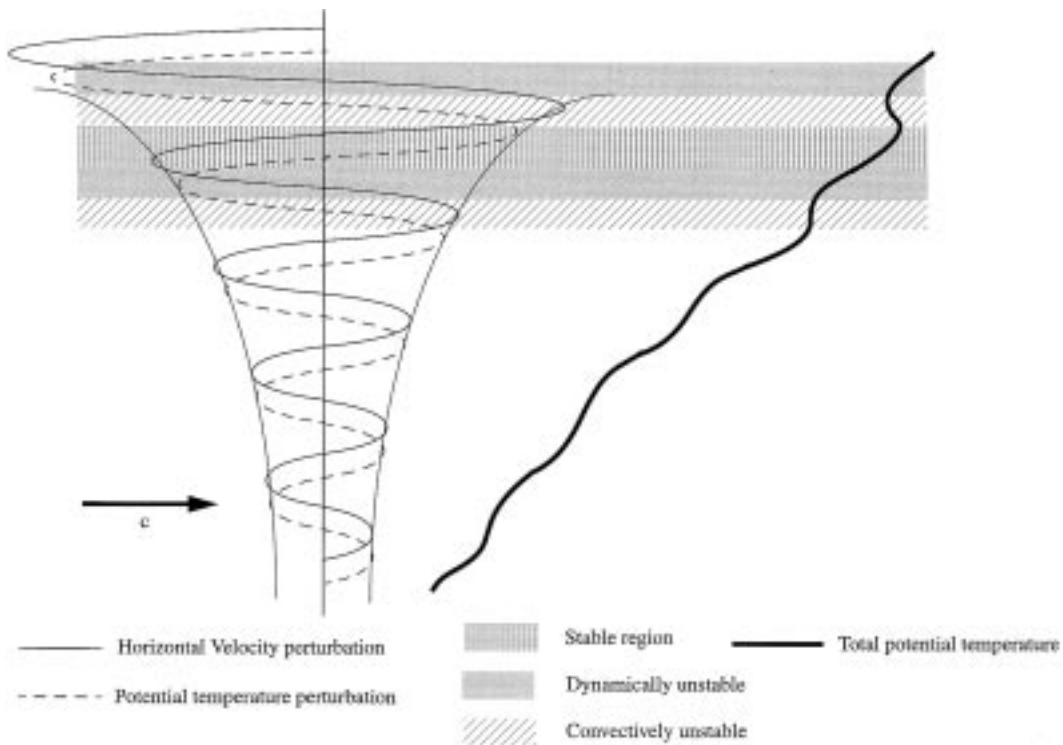
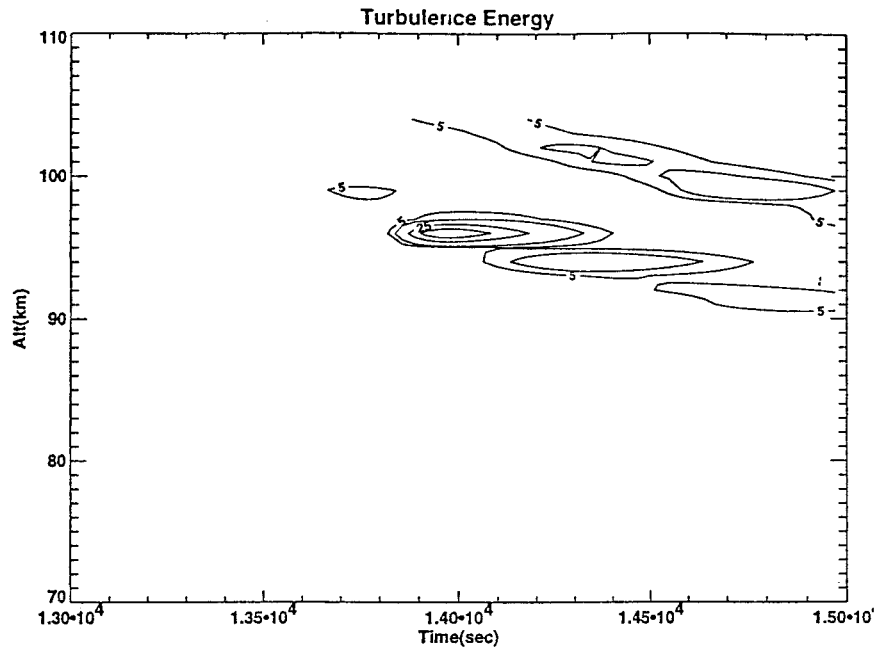
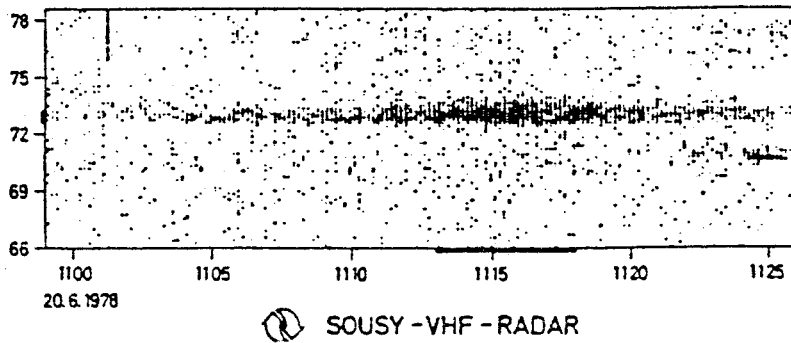


FIG. 10. Schematic plot of the stability of a gravity wave. Horizontal velocity and potential temperature perturbation are plotted on the left according to the linear gravity wave dispersion relation, and the corresponding total potential temperature is plotted on the right.



(a)



(b)

FIG. 11. Turbulence energy (a) at the onset of wave instability as calculated from the model (contour interval: $10 \text{ m}^2 \text{ s}^{-2}$) and (b) measured by the SOUSY radar (Röttger et al. 1979, copyright by the American Geophysical Union).

to altitude are largest with an opposite sign and the diffusion is strongest.

By examining the budget of mass, energy, and momentum flux, and by comparing the model results under small perturbation conditions with the linear analytic results, the dynamics model is found to be satisfactory in the linear domain. In the next section, the model will be applied to finite amplitude and unstable cases along with the turbulence closure.

b. Gravity wave breaking

To study the process of wave-induced instability, and to compare the effects of the turbulence and turbulence

model in the process, two otherwise identical experiments are carried out: one without the turbulence model (case 2) and the other (case 3) with the turbulence model. Both experiments are set up in the same way as case 1, except that a realistic temperature profile, instead of an isothermal atmosphere, is used in the present experiments, and the amplitude of the vertical velocity perturbation is larger (0.1 m s^{-1}).

Figure 3 shows the potential temperature fields at 9900, 10 500, 11 100, 11 700, 12 300, and 12 900 s for case 2. At about 10 000 s, the potential temperature between 100 and 120 km steepens significantly, and at 10 500 s, the potential temperature overturning begins, first at the isotherm of potential temperature 3.31×10^4

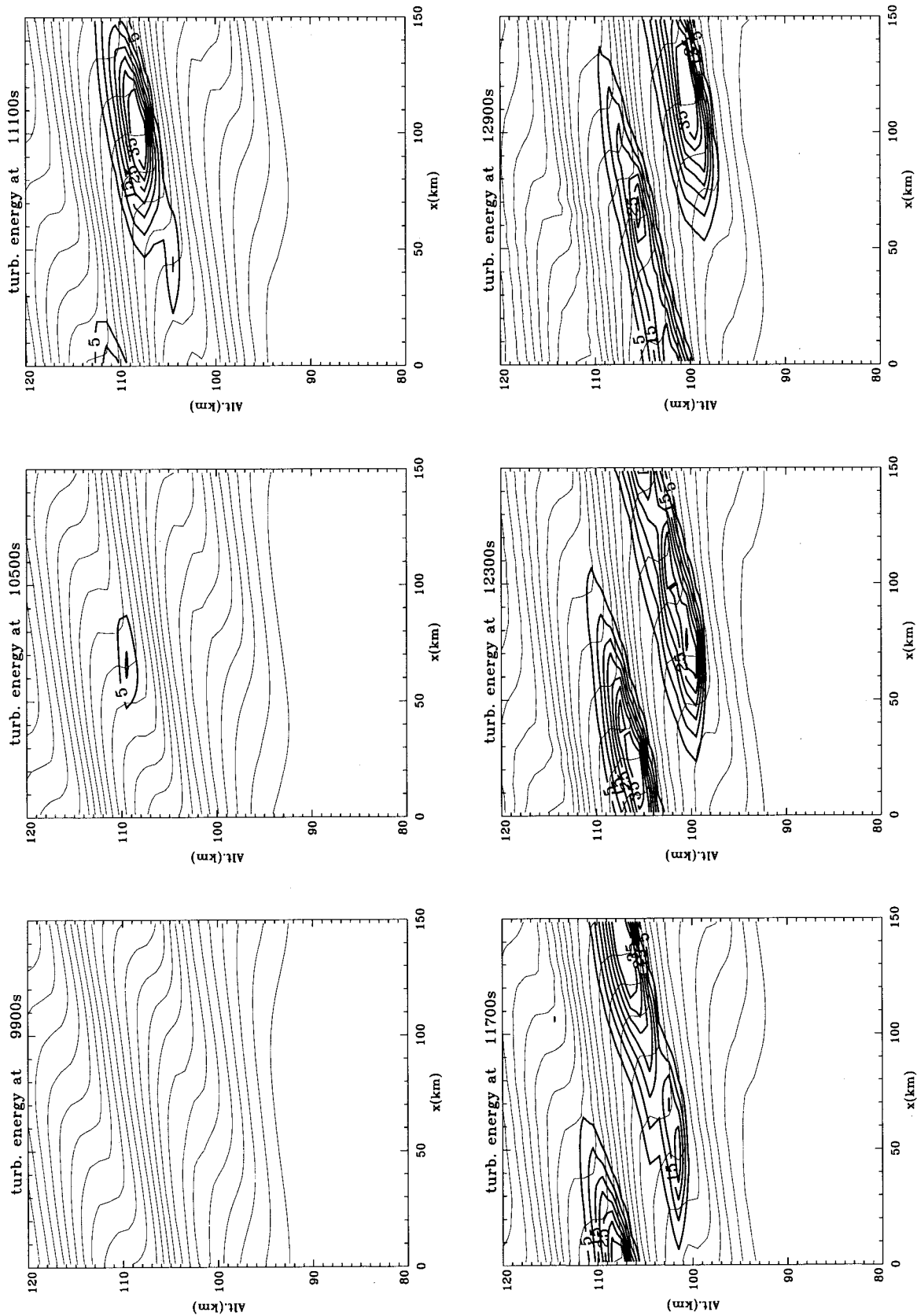


FIG. 12. Thick contour lines, turbulence energy structures at the same time steps as in Fig. 6; contour interval is $5 \text{ m}^2 \text{ s}^{-2}$. Thin contour lines, potential temperature fields, the same as those shown in Fig. 6.

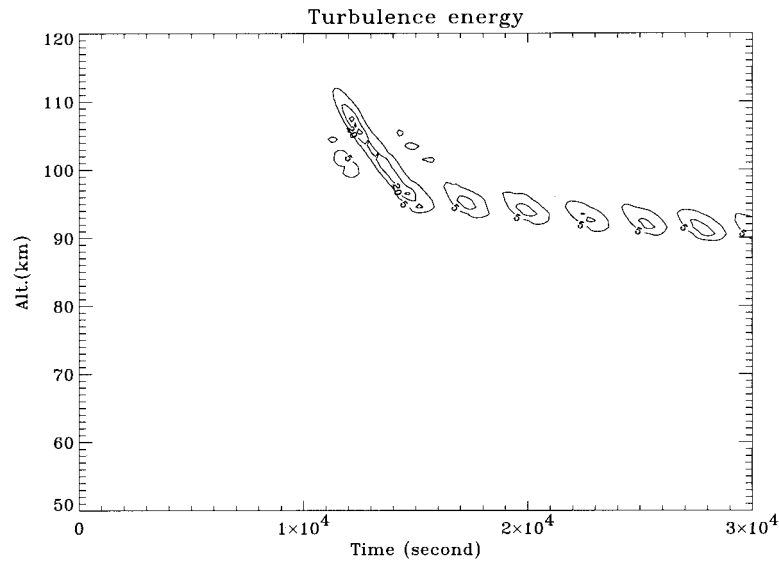


FIG. 13. Evolution of the wave-induced turbulence energy as a function of time and altitude at one horizontal location. From 11 000 to 16 000 s, convective instability due to the wave is dominant; thereafter, dynamical instability due to the induced mean wind shear is more significant. Contour interval: $15 \text{ m}^2 \text{ s}^{-2}$.

K (corresponding to contour value 4.52). This overturning continues and the depth of the overturning grows larger, until it breaks down due to convection.

The vertical velocity fields at these times are shown in Fig. 4. As the potential temperature steepens and begins to overturn, small cells can be observed in the vertical velocity field in the corresponding regions, but the cells do not become apparent until about 600 s after the overturning is first observed. The horizontal scale of the convective cells is about 7.5 km, and the vertical scale is initially 5 km and can grow to more than 10 km (notice that in Fig. 4 the scales and contour intervals for the lower panel plots are larger than those at the upper panel). The vertical velocity amplitude continues growing after wave breaking, and Fig. 5 demonstrates this by the vertical profiles of vertical velocity amplitude at consecutive time steps. This growth indicates the irrelevance of the model result: the stability of the wave is not effectively restored and it contradicts the observation of a saturated wave structure (Theon et al. 1967). It is evident that none of the three-dimensional features can be resolved by the model after wave breaking. Furthermore, the numerical resolution in our study is far too coarse to directly resolve turbulence. If we take the horizontal velocity perturbation at breaking as the characteristic velocity $U \sim 50 \text{ m s}^{-1}$, vertical wavelength as the length scale $L \sim 10\,000 \text{ m}$, and the kinematic viscosity at 110 km is about $10 \text{ m}^2 \text{ s}^{-1}$, then the Reynolds number at the initial breaking region ($\sim 110 \text{ km}$) is about 5×10^4 and the “inner” scale of the turbulence is $\sim \text{Re}^{-3/4} L \sim 3 \text{ m}$ (e.g., Tennekes and Lumley 1972), which is much smaller than the spatial resolution in our simulation. Therefore, the dynamical processes of the

subgrid motion and their effects on the wave and mean flow cannot be directly resolved. This, along with the inability to resolve the three-dimensional features, leads to the false accumulation of wave and mean flow energy.

The same quantities are examined in case 3. Figure 6 shows the potential temperature fields at the same time steps as those shown in Fig. 3. The potential temperature fields in the two experiments are identical until 11 000 s. After wave breaking the overturning is much weaker in case 3 than that in case 2. In fact, the gradient of the potential temperature at maximum steepening after wave breaking is almost always very close to zero in case 3. The maximum steepening gradually moves to lower altitude, while the potential temperature gradient above is restored to larger values, indicating that the static structure becomes more stable. On the other hand, in case 2, the negative potential temperature gradient persists. Furthermore, by comparing Figs. 7 and 4, it can be seen that the vertical velocity fields in these two experiments are identical until 11 000 s. After wave breaking, cells can be observed in the present case with similar scales and at the same locations as in case 3, but the amplitude is smaller and does not significantly increase with time. Figure 8 shows the profiles of the vertical velocity amplitude, and it approaches a constant in the wave-breaking region. This is a characteristic feature of wave saturation and also an assumption for the linear saturation theory, showing that by using the turbulence closure the model is able to simulate wave amplitude saturation in the breaking region. This is also an indication that the turbulence model has removed the proper amount of energy from the wave and the mean field.

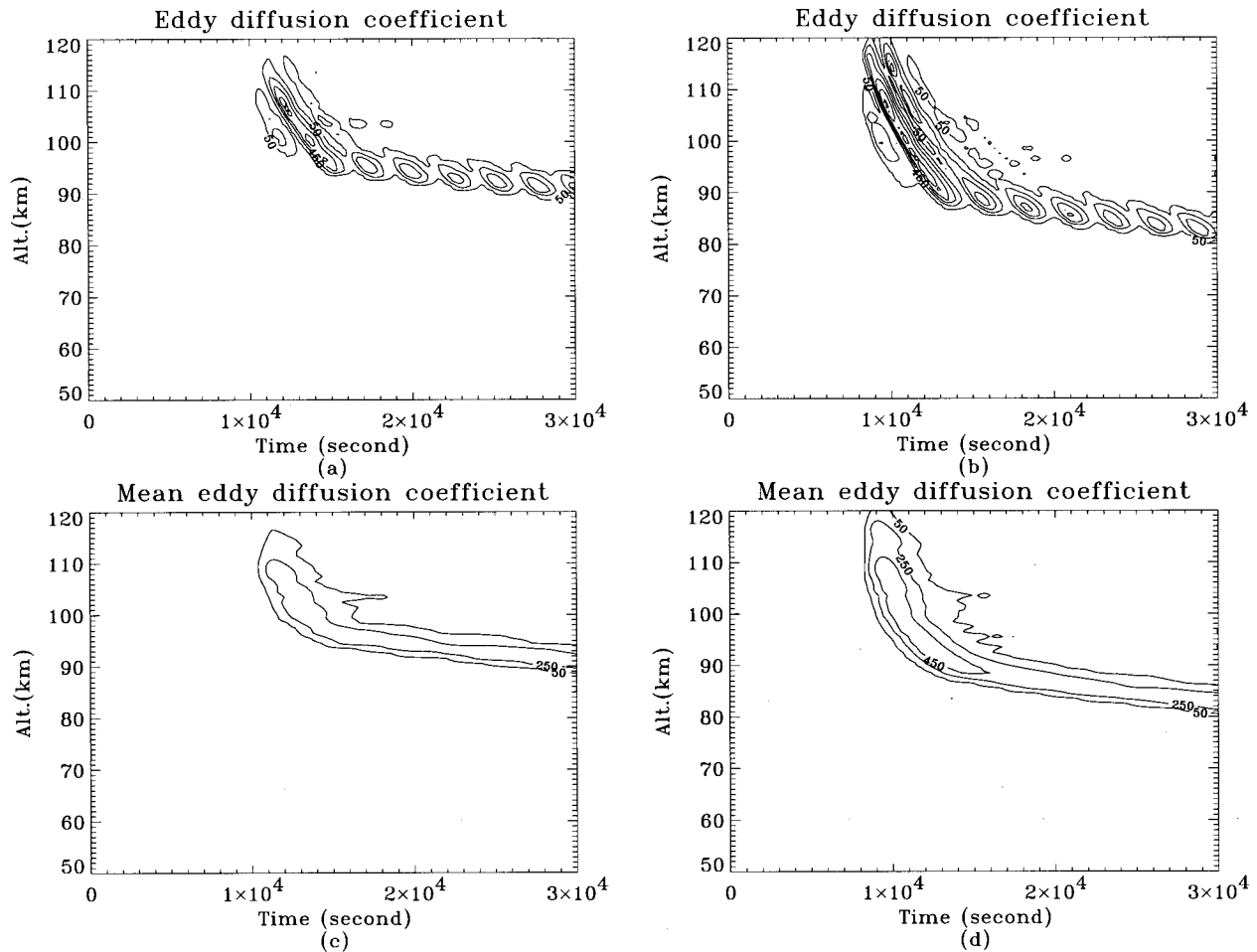


FIG. 14. Eddy diffusion coefficient of two comparing cases; (a) at one horizontal position, when the vertical velocity perturbation at lower boundary $w_0 = 0.1 \text{ m s}^{-1}$ (case 3); (b) at one horizontal position, when $w_0 = 0.2 \text{ m s}^{-1}$ (case 4); (c) averaged over one horizontal wavelength for case 3; (d) averaged over one horizontal wavelength for case 4. The contour interval for all four plots is $200 \text{ m}^2 \text{ s}^{-1}$.

The linear saturation theory postulated by Lindzen (1981) predicted that the vertical velocity amplitude at the breaking level is approximately

$$|w_{\text{break}}| \approx \frac{\omega}{k_z}. \quad (14)$$

In this case, the vertical wavelength at the breaking level is about 12 km, and the frequency of the wave is 2500 s; thus according to Eq. (14) the vertical velocity at the saturation level is 4.8 m s^{-1} , which is about the same with the numerical results. This is, however, a crude comparison and the process is more complicated. The waves breaking initially at higher altitudes are faster components with phase speed larger than 60 m s^{-1} . Furthermore, there is already a mean flow acceleration by wave transience before breaking.

The mean horizontal velocity increases as a result of wave breaking. Figure 9 is the kinetic energy budget for case 3 during this process. The kinetic energy of the mean flow (dotted line) increases almost linearly with

time after 14 000 s, which implies that the rate of energy transfer from the wave to the mean flow is approximately a constant after wave breaking. Furthermore, this rate is roughly equal to the rate of the kinetic energy input from the lower boundary. This can be verified by the observation that the slope of the dotted line between 14 000 and 25 000 s is approximately equal to the slope of the solid line during the wave buildup period (7000–10 000 s). The latter reflects the rate of kinetic energy input from the lower boundary, because during the wave buildup the bulk of the wave is in the effective computational domain and little energy leaks from its top boundary, thus the net change of kinetic energy comes from the lower-boundary input. The wave kinetic energy, on the other hand, decreases after reaching its peak at about 13 000 s, which might be due to the energy lost to turbulence. After 18 000 s, the wave kinetic energy is close to a constant, and it may be concluded that the energy transfer between the wave, the mean flow, and turbulence reaches an equilibrium state. More de-

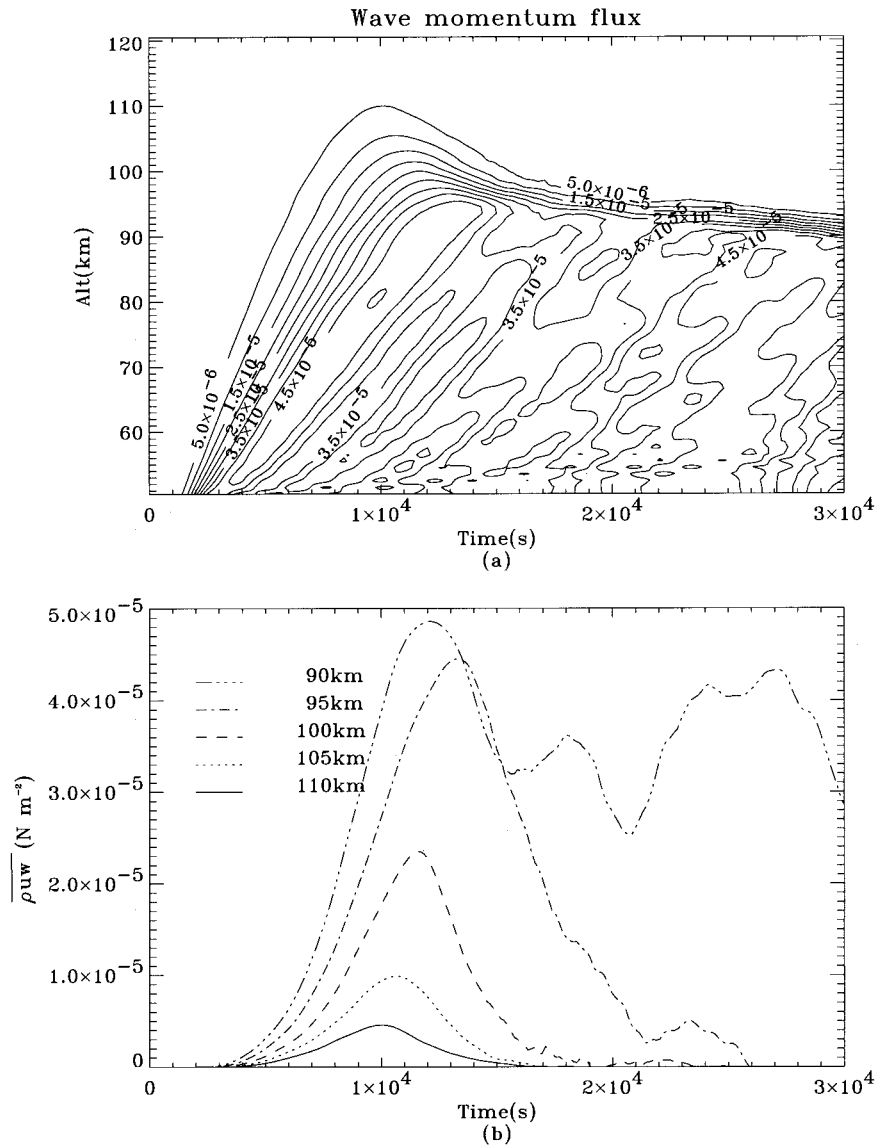


FIG. 15. A breaking gravity wave momentum flux (a) as function of time and altitude, and (b) slices at five different altitudes. The momentum flux decreases after wave breaking.

tailed discussion of the mean flow structure will be given after the investigation of the turbulence structures, so that the wave momentum and heat flux can be compared with the turbulence momentum and heat flux.

c. Turbulence due to gravity wave breaking

The generation of turbulence is determined by the wind and the temperature fields of the wave. According to the linear dispersion relation of the internal gravity wave, the phase of the horizontal velocity leads the phase of potential temperature perturbation by about a quarter of a vertical wavelength in the vertical direction, as shown in Fig. 10. When the wave amplitude becomes large, the wave stability can be roughly divided into

three categories: convective instability when the total potential temperature gradient becomes zero or negative; dynamical instability when the shear of the velocity perturbation becomes large while the gradient of the potential temperature perturbation is small; stable when the gradient of the potential temperature perturbation is large and the wind shear is small. It can thus be expected that the turbulence be nonuniform and advectively and diffusively transported along and across the wave phase line.

The relation between the wave-induced turbulence and the wave is first examined at the onset of the turbulence. The turbulence structure in this process can be seen in Fig. 11a. The turbulence generated at 96 km at 1.38×10^4 s grows to its peak at 1.40×10^4 s, then

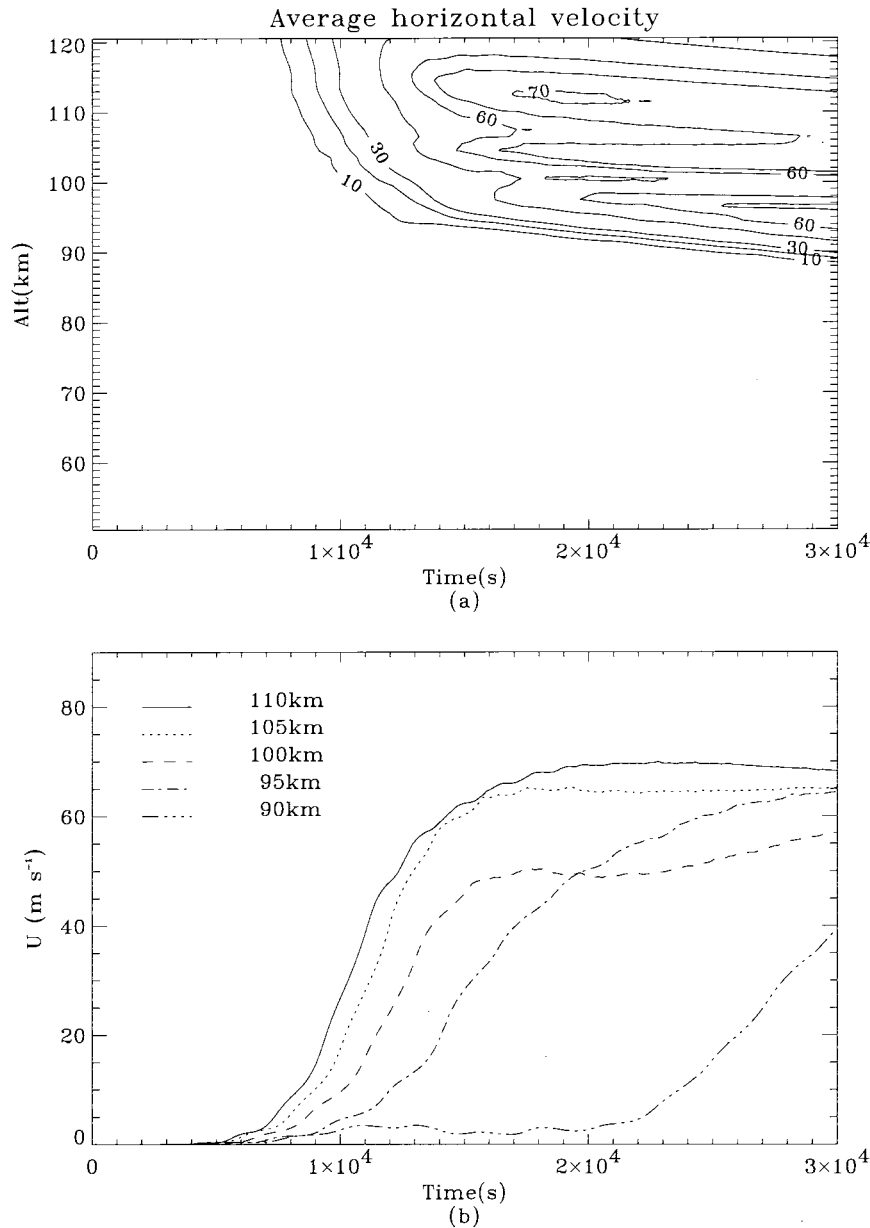


FIG. 16. Average horizontal velocity (a) as a function of time and altitude, and (b) at five different altitudes. At each altitude, the average horizontal velocity approaches a constant after wave breaking. Shear develops due to the difference of acceleration rate between the altitudes.

decays and vanishes at about 1.44×10^4 s. The lifetime of the turbulence is about 10 min, with a vertical scale of about 3 km, and the average vertical position of the turbulence does not change with time. After the turbulence energy in this region begins to decay, but before it vanishes, there is another area below, at 94 km, where turbulence starts to grow. The turbulence structure is tuned by the wave structure: the bands of turbulence areas correspond to the unstable wave regions, separated by stable ones where turbulence is strongly suppressed. The vertical distance between the center of the bands

is about 10 km, which is close to the vertical wavelength.

Thin-layer turbulence structures similar to the numerical results have been observed in previous radar studies. Figure 11b is the turbulence energy measured by the SOUSY very high frequency (VHF) radar by Röttger et al. (1979). The lifetime of the turbulence at 73 km is about 20 min, with clear growing and decaying periods; the vertical scale is about 1.5 km; and the average vertical position does not change. During the decay, another turbulence area appears around 71 km.

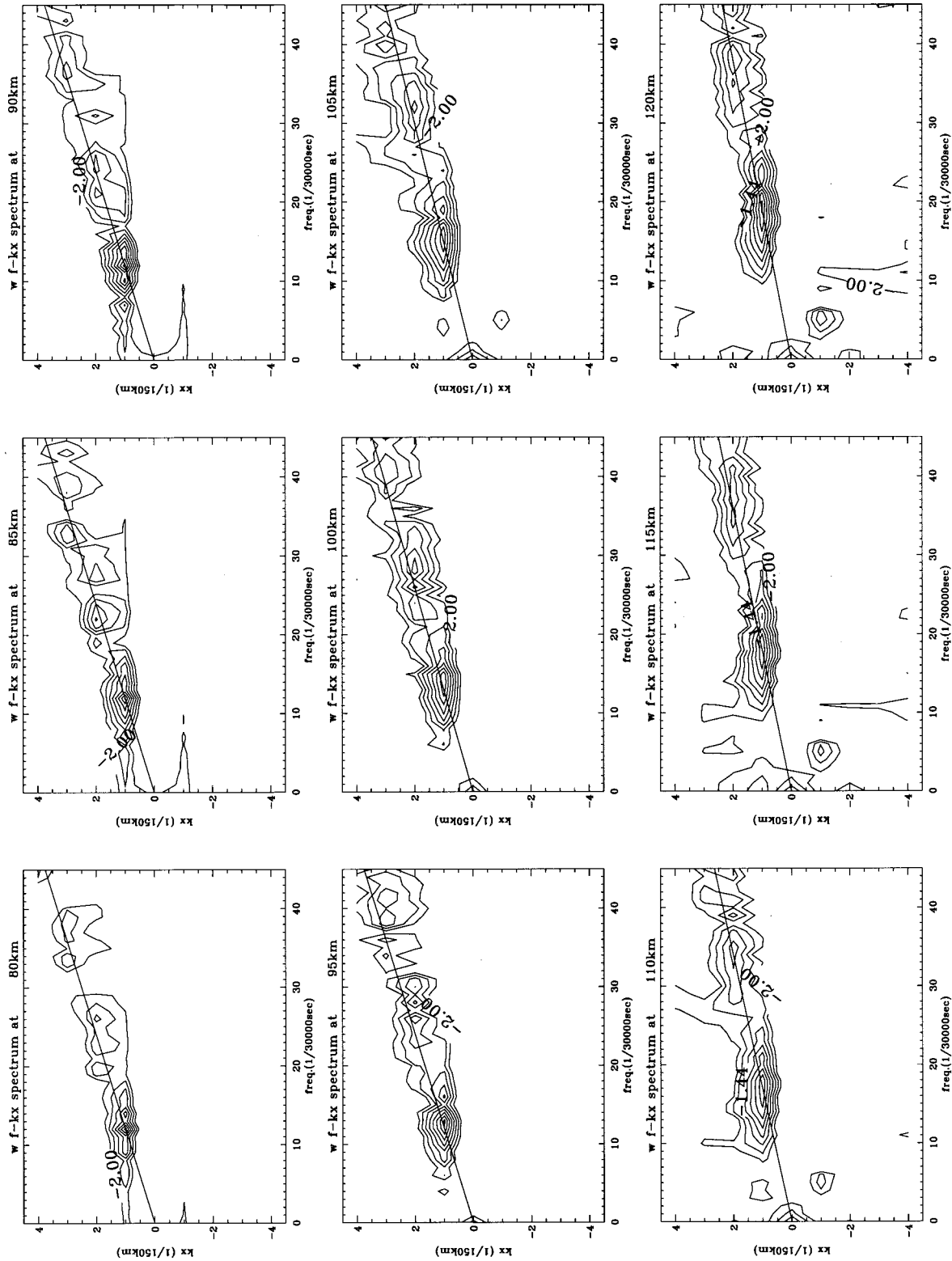


FIG. 17. Frequency and horizontal wavenumber spectrum of vertical velocity at nine different altitudes. The straight line connects the origin and the mode with maximum amplitude, whose reciprocal is the phase speed. The contour plots are on the same log scale.

Such similarity suggests an explanation for the formation of the observed turbulence structure by relating them quantitatively to the gravity wave–breaking process.

Figure 12 shows the turbulence density in case 3 (thick contour line). The potential temperature fields, the same as those shown in Fig. 6, are overplotted here using thin contour lines for comparison. It can be seen that the location of the maximum turbulence density matches that of the potential temperature steepening and overturning, indicating the dominant role of convective instability in the generation of turbulence. It should also be noted that the turbulence density is not symmetric with respect to its peak value: the turbulence layer is thinner and has a larger gradient on the right-hand side (i.e., the propagating side) of the peak than that on the left-hand side (the wake of the turbulence). It is also interesting to notice that the temporal and spatial structures of the turbulence shown in Figs. 11a and 12 are quite similar to the mean eddy kinetic energy structures and their evolution shown by the three-dimensional DNS results (Fritts et al. 1996).

After wave breaking, the mean wind acceleration produces a strong descending shear layer. Therefore, the shear becomes more dominant for generating turbulence. Figure 13 shows the temporal evolution of the turbulence structure at a fixed horizontal location in case 3. The peak value of the turbulence energy, about $35 \text{ m}^2 \text{ s}^{-2}$, occurs at 110 km and corresponds to the overturning region. This region moves downward with the phase line of the wave. When the unstable region moves downward, the maximum potential temperature gradient and the maximum wave shear decrease due to the smaller wave amplitude at lower altitudes, but the mean shear due to wave acceleration increases. The mean shear will become large enough such that the controlling factor of the dynamical instability switches from wave shear to mean shear at around 15 000 s and 95 km. After this, the descent of the maximum turbulence is determined by the mean shear, while still modulated by the wave.

The eddy diffusion coefficients can be calculated from the turbulence energy density by Eqs. (10) and (11) for case 3 and a comparing case 4, which is similar to the case 3 except its perturbation amplitude is twice as large (0.2 m s^{-1}). Figure 14a is the temporal evolution of the eddy diffusion coefficient K_M at a fixed horizontal location for case 3. The maximum K_M is about $700 \text{ m}^2 \text{ s}^{-1}$ during the convective breakdown, and about $500\text{--}600 \text{ m}^2 \text{ s}^{-1}$ in the strong shear region. The average value of K_M over one horizontal wavelength is shown in Fig. 14c, with peak values of about 360 and $300 \text{ m}^2 \text{ s}^{-1}$ in the shear layer. Figures 14b, d are results from case 4. The initial overturning is still around 110 km, but its occurrence is earlier. The maximum value of K_M is about $1000 \text{ m}^2 \text{ s}^{-1}$ and $500\text{--}650 \text{ m}^2 \text{ s}^{-1}$ in the shear layer. The peak of the average K_M is about $570 \text{ m}^2 \text{ s}^{-1}$ and $300 \text{ m}^2 \text{ s}^{-1}$ in the shear layer.

In the linear saturation theory, Lindzen (1981) as-

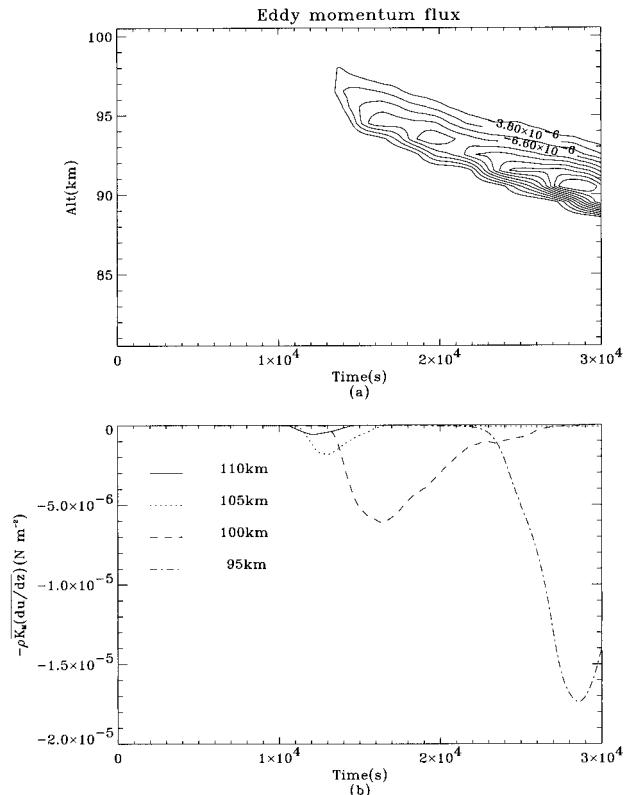


FIG. 18. Turbulence momentum flux (a) as a function of time and altitude and (b) at four different altitudes. It is downward and the values increase with the shear of the average horizontal velocity.

sumed a uniform eddy diffusion coefficient distribution and obtained the following expression for K_M ($=K_H$) due to gravity wave breaking:

$$K_M \approx \frac{k_x(c-u)^4}{N^3(1+k_y^2/k_x^2)^{3/2}} \frac{1}{2H}. \quad (15)$$

In both cases considered here at the initial breaking at 110 km, the intrinsic phase speed $c-u = (85-20) \text{ m s}^{-1} = 65 \text{ m s}^{-1}$, due to the fast gravity wave component and transience acceleration; horizontal wavenumbers in x and y directions, $k_x = 2\pi/(150 \text{ km}) = 4.19 \times 10^{-5} \text{ m}^{-1}$, $k_y = 0$; the Brunt–Väisälä frequency $N \approx 2\pi/(250 \text{ s}) = 2.51 \times 10^{-2} \text{ s}^{-1}$; and the scale height $H \approx 7300 \text{ m}$; thus $K_M = 3.24 \times 10^3 \text{ m}^2 \text{ s}^{-1}$, which is much larger than those from the numerical experiments. Therefore, in the cases studied here, Lindzen's parameterization is an overestimate of the mean wave-induced turbulence mixing. The overestimate may be due to the fact that the wave amplitude from linear theory is not reached at the breaking level due to wave transience, nonlinearity, and/or viscosity. That the turbulence is local instead of uniform might also contribute to the discrepancy. The eddy diffusion coefficients from the two experiments are about the same in the strong shear region where c is very close to u . Here Eq. (15) may be invalid because of the strong shear.

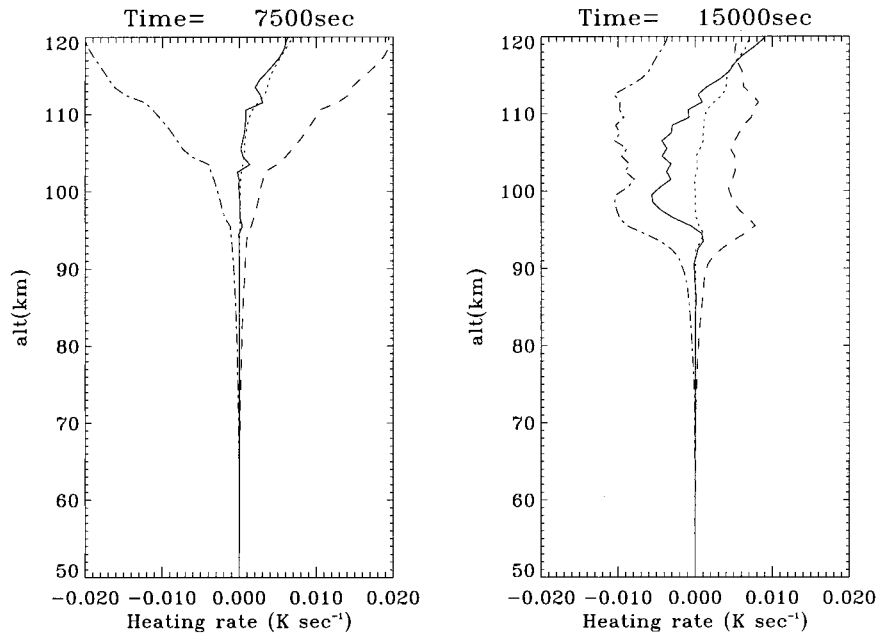


FIG. 19. Heating rates (a) before and (b) after wave breaking. Solid line; total heating rate; dashed line, warm advection (vertical advection); dashed-dotted line, cold advection (horizontal advection); dotted line, eddy and molecular diffusion.

It should be noted that the eddy diffusion coefficients K_M and K_H , and the Prandtl number Pr_i are calculated from the turbulence closure model and parameterize the effects of the subgrid scale (<1 km) turbulence motion, and the quantitative test of such parameterization should be made by comparison with other studies.

d. Wave breaking impacts on the mean flow

The mean flow acceleration and heating are directly related to the convergence of the momentum and heat flux, respectively. These fluxes may undergo significant change as a result of wave breaking and the wave-induced turbulence. The gravity wave momentum flux of case 3 is shown in Fig. 15, where Fig. 15a is the contour plot showing the momentum flux as a function of time and altitude and Fig. 15b shows the momentum flux at five different altitudes from 90 to 110 km, with 5-km intervals. The corresponding mean velocity is shown in Figs. 16a and 16b. The evolution of the wave momentum flux and mean flow has three stages, with different controlling mechanisms. The first stage is before 10 000 s, when the wave builds up and the momentum flux grows with time at all altitudes. It can be seen that the upward momentum flux at each level increases with time during wave growth, and the rate of increase is larger at lower altitudes. Therefore, the wave momentum flux decreases with altitude. This results in the convergence of momentum flux and the transient acceleration of the mean flow.

The second stage is the initial wave breaking during the period from 10 000 to 15 000 s between 90 and 120

km due to convectively unstable wave structures. Figure 13 shows that at this stage the breaking region descends with the wave front, and from Fig. 15b it can be seen that the momentum flux decreases from a maximum value after the wave breaks down at each altitude. Therefore, the maximum momentum flux convergence region descends with the wave phase front and causes the mean flow acceleration at lower altitudes. Because there is almost no acceleration in the stable region, the difference leads to an increasing shear layer in the lower breaking region.

During the third stage, instability due to the strong mean shear layer becomes the dominant mechanism, because the wave is more stable at lower altitudes due to the smaller wave amplitude. The wave momentum flux decreases at the breaking level in the shear layer and thus increases the convergence of momentum flux between this breaking level and the stable region below. This accelerates the mean flow and extends the shear layer to lower altitudes. On the other hand, the momentum flux above the breaking level decreases and tends to zero (Fig. 15b); therefore, its vertical divergence also tends to zero and so does the acceleration rate in these regions. The peak value of the average horizontal velocity in the breaking region can be as large as 70 m s^{-1} (at about 110 km after wave breaking). This is likely due to dispersion: the faster waves with higher frequency and larger phase and group velocity from wave transience break first if their amplitudes are large enough. Figure 17 is the frequency-horizontal wavenumber spectrum of the vertical velocity at nine altitudes from 80 to 120 km with 5-km

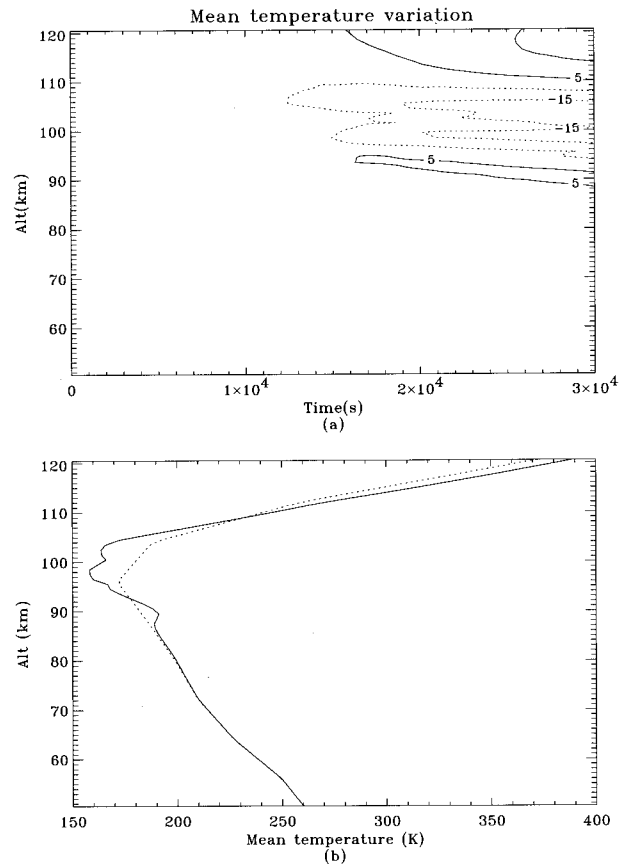
intervals (plotted on the same log scale). At 80 km, the wave is stable during the whole simulation period, and it can be seen that the single dominant wave mode has a horizontal wavelength of 150 km (wavenumber 1) and a wave period 2500 s (frequency number 12); therefore, the phase velocity is 60 m s^{-1} and the wave characteristics are the same with those of the source at the lower boundary. The line in the plot connects the origin and the dominant wave mode and has a slope of k_{x0}/ω_0 , where k_{x0} and ω_0 are the wavenumber and frequency of the dominant mode in radians, respectively. The slope of this line is thus the reciprocal of the wave horizontal phase velocity. It can also be seen that this line approximately connects the locally dominant modes, which shows the wave dispersion relation and that the horizontal group velocity of the wave is equal to its corresponding phase velocity, $d\omega/dk_x = \omega/k_x$. The frequency of the dominant wave increases with altitude while its horizontal wavenumber remains the same, which is consistent with the dispersion of the wave. Therefore, the wave horizontal phase velocity and group velocity are larger at higher altitudes. The acceleration thus generated will also be larger than 60 m s^{-1} , though it is difficult to ascertain how important wave self-acceleration is. A similar phenomenon has also been observed by Walterscheid and Schubert (1990) in their numerical experiment. Figure 17 also shows that the single dominant mode expands and becomes a dominant spectrum at higher altitude. Modes with smaller spatial and temporal scales due to wave breaking can also be seen at higher altitudes in this figure.

The momentum transport due to wave-induced turbulence is calculated from the turbulence model:

$$\overline{\rho \langle u''w'' \rangle} = -\rho K_M \frac{\partial \overline{u}}{\partial z}, \quad (16)$$

where the overbar is for averaging over one horizontal wavelength. Figure 18a shows the development of turbulence momentum flux, and Fig. 18b the fluxes at four different altitudes between 95 and 110 km with 5-km intervals. The turbulence momentum flux is insignificant during the initial breaking relative to the wave momentum flux. When the mean wind shear becomes stronger, the downward turbulence momentum flux increases. At 110 km, the peak value of the turbulence momentum flux is $-5.0 \times 10^{-7} \text{ N m}^{-2}$, about 10% of the maximum upward wave momentum flux at that level. At 100 km, the peak value is $-6.0 \times 10^{-6} \text{ N m}^{-2}$ and is approximately equal to the upward wave momentum flux at that altitude and time. Therefore, the turbulence diffusion of the strong shear becomes more important at lower altitudes.

From Fig. 16b, it can be estimated that the maximum acceleration rate is about $40 \text{ m s}^{-1} \text{ h}^{-1}$ at 110 km from 10 000 to 12 000 s. This is smaller than the acceleration rate calculated from the linear saturation theory, which



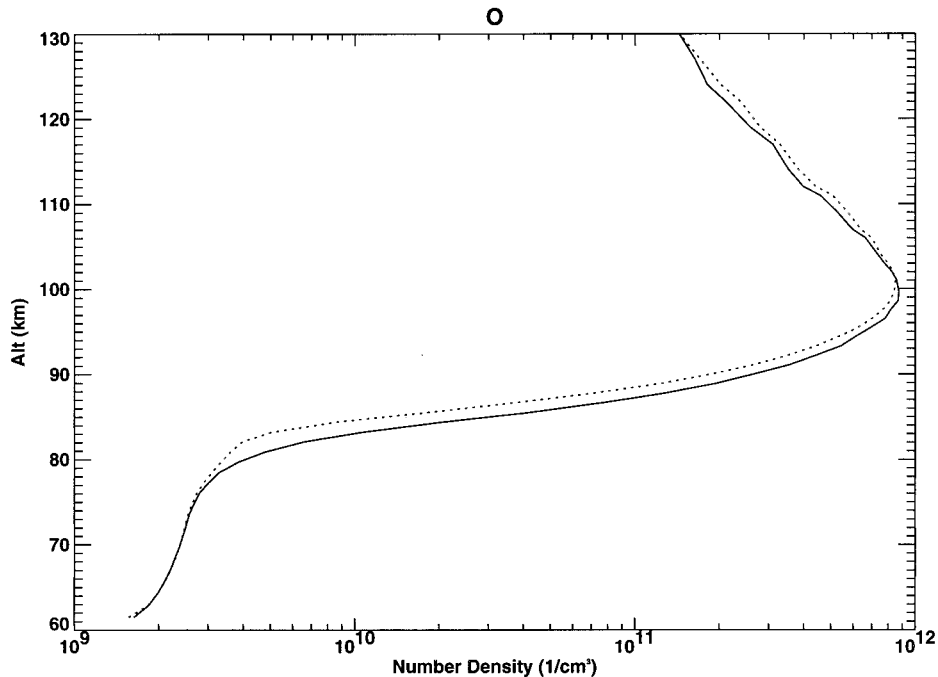


FIG. 21. Profile of atomic oxygen number density at $t = 0$ (dotted line) and $t = 18\,000$ (solid line). The relative increase at 85 km is about 100%.

altitude, and Fig. 20b the mean temperature profile at $t = 0$ and $t = 30\,000$ s.

The temperature drops significantly (15–20 K) in most of the wave-breaking region, except at the lower altitudes where the shear is strong. The temperature there increases by about 5 K due to the convergence of turbulence heat flux. The turbulence viscous heating, on the other hand, is much smaller (not shown in the plot). The lower thermosphere above the wave-breaking region is significantly heated, mostly due to molecular diffusion.

e. Atmospheric compositional change due to wave breaking

In this experiment, a gravity wave packet breaks at 11 000 s between 85 and 115 km, and then moves downward. The eddy diffusion coefficient averaged over one horizontal wavelength reaches a maximum of about $1100\text{ m}^2\text{ s}^{-1}$ at the beginning of the breaking, and the local value can be twice as large. The strong eddy diffusion can significantly enhance the downward transport of atomic oxygen. Figure 21 shows the profiles of atomic oxygen distribution at $t = 0$ and $t = 18\,000$ s. The number density of O increases between 70 km and 100 km where it peaks, but decreases above 100 km. Both changes take place after wave breaking begins at 11 000 s. The maximum increase is between 15 000 and 18 000 s around 93 km, and the increase is more than $9 \times 10^{10}\text{ cm}^{-3}$, about 23% of the initial value at that height. The largest percentage increase, however, is around 85 km,

where the number density doubles compared with the initial value. The decrease above 100 km maximizes around 110 km, at about $5 \times 10^{10}\text{ cm}^{-3}$, which is 10% of the initial number density at that altitude.

Other chemical species are also affected, both by the wave and eddy transport and by chemical reaction with other species. Figure 22 shows the number density percentage change of O_3 , OH, H, and HO_2 . The changes of the ozone number density closely correlate with the changes of atomic oxygen: there is little change at 100 km, a significant increase between 70 and 100 km (maximum of about 200%), and a decrease above 100 km. This also shows that the atomic oxygen variation is the dominant factor in determining the distribution of ozone, while dynamical transport is only of secondary importance. The increase of O and O_3 number density around 85 km after wave breaking causes the loss of OH and HO_2 in the same region. The maximum percentage decrease of OH is 50% at around 15 000 s, and the decrease is even larger for HO_2 , 60%. The atomic hydrogen, however, increases slightly in the same region. The differences between the variation of these three species can be related to the major reactions between O and the hydrogen species (Roble 1995).

4. Conclusions

In this work, a self-consistent model system has been developed that couples a dynamics model, a turbulence model, and a chemistry model. The dynamics model is able to simulate the nonlinear gravity wave propagation

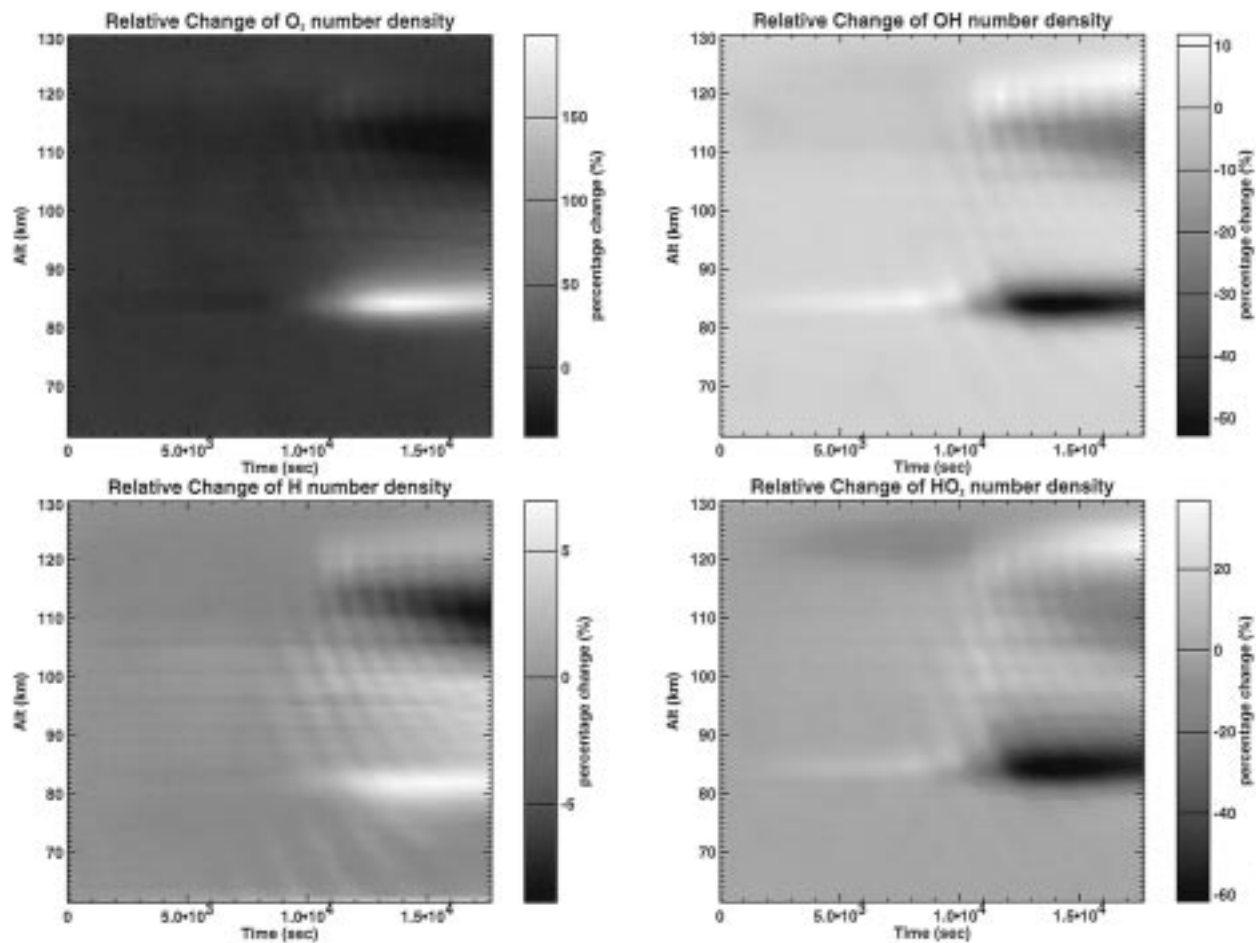


FIG. 22. Relative variations of O_3 , OH, H, and HO_2 before and after wave breaking. The maximum increase of is almost 200% at 85 km.

in an atmosphere with a realistic background temperature and molecular diffusion, as well as an adjustable background wind. The turbulence model parameterizes subgrid interactions after the onset of instability and the enhanced mixing due to the three-dimensional turbulence. The chemistry model is used to calculate the change of compositional structures caused by advection, diffusion, and temperature. Therefore, the simultaneous interactions among breaking gravity wave, turbulence, mean flow, and the mesosphere–lower-thermosphere chemistry may be studied using this model system. From the simulations, the following conclusions can be derived.

In previous two-dimensional models, the strength and the persisting time of the potential temperature supersaturation are much stronger and longer than those predicted by a three-dimensional model. This work demonstrates that this difficulty might be overcome if a properly adjusted turbulence closure model is applied. By using the 2.5-level Mellor–Yamada turbulence model, the unrealistic strong supersaturation is eliminated and the local turbulence is efficient in restoring the negative potential temperature gradient to a near-zero value. On

the other hand, the quantitative capability of such a model can only be fully exploited with more elaborate model adjustment according to observation results and DNS–LES results that would have a better description of the turbulence physics more relevant to the problems of wave breaking. The major difficulty is the lack of a benchmark database for the tuning of the turbulence model.

The model demonstrates that the amplitude of the wave perturbation is nearly independent of altitude in the wave-breaking region (i.e., amplitude saturation), which is consistent with what has been assumed in the linear saturation theory.

The gravity wave breaking starts from the faster wave components at higher altitudes. At the beginning of wave breaking, the wave thermal structure is the determining factor of wave instability in two senses: 1) the negative potential temperature gradient leads to convective instability and 2) the large positive potential temperature gradient has a stabilizing effect and suppresses turbulence. The model shows that the turbulence thus generated exhibits layer structures that have similar spatial and temporal characteristics to radar observa-

tions. Because of the determining role of wave stability during this period, the region of maximum turbulence moves downward with the wave phase line, while turbulence at higher altitudes decays with time.

At lower altitudes, the wave becomes more convectively stable due to the smaller perturbation amplitude. At the same time, the shear due to the mean flow acceleration increases and this shear becomes the dominant source for instability and turbulence. The turbulence also moves downward as the shear layer descends, but at a much slower rate than the vertical phase velocity of the wave.

Eddy diffusion coefficients are calculated from the turbulence model. The numerical results show that they are dependent on the wave characteristics and correspond closely to the turbulence structures. The mean eddy diffusion coefficients averaged over one horizontal wavelength are compared with the results from the linear saturation theory, and it is found that the model results are smaller than the theoretical results in the cases considered.

Gravity wave breaking and the wave-induced turbulence reduce the upward wave momentum flux above the breaking level and produce additional mean flow acceleration. The acceleration at each wave-breaking altitude continues but at an ever slower rate, because as the wave breaks down at lower altitudes, more wave momentum is deposited at lower altitudes. The mean horizontal velocity in this region is approximately a constant when both the wave momentum flux and its gradient approach zero. Both the wave-breaking level and the maximum acceleration level descend with the phase line of the wave when wave instability dominates. At the same time, the mean wind shear at the boundary between the breaking and the stable regions becomes larger and eventually the flow becomes unstable in the shear layer. The descending rate of this layer, and thus the descending rate of the maximum accelerating level, are much slower than the vertical phase speed.

The mean flow velocity in the breaking region is larger at higher altitudes and decreases to about 60 m s^{-1} above the shear layer. This is probably due to the dispersion of the gravity wave components during the transient period of its generation. The faster components with large enough amplitude will break first and the mean wind velocity produced by these components can be larger than 60 m s^{-1} , the phase speed of the steady component. The acceleration rate from the model is again smaller than the linear saturation theory prediction.

The balance between the cold advection (horizontal advection) and warm advection (vertical advection) is broken after wave breaking. This causes a net cooling effect in most of the breaking region, except that turbulence heating is more significant at lower altitudes with the strong shear.

Gravity wave breaking and the wave-induced turbulence enhance the downward transport of the atomic

oxygen, and the number density of the atomic oxygen significantly increases below the peak value at 100 km, while it decreases above. The increase of the atomic oxygen number density below 100 km leads to the increase in the ozone number density in the same region and causes changes in other chemical species.

Acknowledgments. The authors would like to acknowledge valuable discussions with and suggestions by Drs. S. J. Jacobs, K. G. Powell, and A. D. Richmond. Reviews and comments by Dr. O. Andreassen and two other anonymous reviewers are gratefully acknowledged. This research is supported by National Aeronautics and Space Administration through Contract NAS 5-27751. H.-L. Liu was supported in part by NASA Grants S-67018-F and S-97239-E to NCAR during the revision of this manuscript.

REFERENCES

- Andreassen, O., C. E. Wasberg, D. C. Fritts, and J. R. Isler, 1994: Gravity wave breaking in two and three dimensions. Part I: Model description and comparison of two-dimensional evolutions. *J. Geophys. Res.*, **99**, 8095–8108.
- Chao, W. C., and M. R. Schoeberl, 1984: A note on the linear approximation of gravity wave saturation in the mesosphere. *J. Atmos. Sci.*, **41**, 1893–1898.
- Coy, L., and D. C. Fritts, 1988: Gravity wave heat fluxes: A Lagrangian approach. *J. Atmos. Sci.*, **45**, 1770–1780.
- Dobosy, R., 1979: Dispersion of atmospheric pollutants in flow over the shorelines of a large body of water. *J. Appl. Meteor.*, **18**, 117–132.
- Dunkerton, T. J., 1987: Effects of nonlinear instability on gravity wave momentum transport. *J. Atmos. Sci.*, **44**, 3188–3209.
- Fritts, D. C., 1985: A numerical study of gravity wave saturation: Nonlinear and multiple wave effects. *J. Atmos. Sci.*, **42**, 2043–2058.
- , and T. J. Dunkerton, 1985: Fluxes of heat and constituents due to convectively unstable gravity waves. *J. Atmos. Sci.*, **42**, 549–556.
- , J. R. Isler, and O. Andreassen, 1994: Gravity wave breaking in two and three dimensions. Part II: Three-dimensional evolution and instability structure. *J. Geophys. Res.*, **99**, 8109–8123.
- , J. F. Garten, and O. Andreassen, 1996: Wave breaking and transition to turbulence in stratified shear flows. *J. Atmos. Sci.*, **53**, 1057–1085.
- , S. Arendt, and O. Andreassen, 1998: Vortex dynamics in a breaking internal gravity wave, II: Vortex interactions and transition to turbulence. *J. Fluid Mech.*, **367**, 47–65.
- Hodges, R. R., 1969: Eddy diffusion coefficients due to instabilities in internal gravity waves. *J. Geophys. Res.*, **74**, 4087–4090.
- Holton, J. R., 1982: The role of gravity wave induced drag and diffusion in the momentum budget of the mesosphere. *J. Atmos. Sci.*, **39**, 791–799.
- , 1983: The influence of gravity wave breaking on the general circulation of the middle atmosphere. *J. Atmos. Sci.*, **40**, 2497–2507.
- Isler, J. R., D. C. Fritts, and O. Andreassen, 1994: Gravity wave breaking in two and three dimensions. Part III: Vortex breaking and transition to isotropy. *J. Geophys. Res.*, **99**, 8125–8137.
- Kaltenbach, H.-J., T. Gertz, and U. Schumann, 1994: Large-eddy simulation of homogeneous turbulence and diffusion in stably stratified shear flow. *J. Fluid Mech.*, **280**, 1–40.
- Klaassen, G. P., and W. R. Peltier, 1985a: The evolution of finite amplitude Kelvin–Helmholtz billows in two spatial dimensions. *J. Atmos. Sci.*, **42**, 1321–1339.

- , and —, 1985b: The onset of turbulence in finite amplitude Kelvin–Helmholtz waves. *J. Fluid Mech.*, **155**, 1–35.
- Klemp, J. B., and R. B. Wilhelmson, 1978a: The simulation of three-dimensional convective storm dynamics. *J. Atmos. Sci.*, **35**, 1070–1096.
- , and —, 1978b: Simulation of right- and left-moving storms produced through storm splitting. *J. Atmos. Sci.*, **35**, 1097–1110.
- Lindzen, R. S., 1981: Turbulence and stress due to gravity wave and tidal breakdown. *J. Geophys. Res.*, **86**, 9707–9714.
- , and J. Forbes, 1983: Turbulence originating from the convectively stable internal waves. *J. Geophys. Res.*, **88**, 6549–6553.
- Mellor, G. L., and H. J. Herring, 1973: A survey of the mean turbulent field closure models. *AIAA J.*, **11**, 590–599.
- , and T. Yamada, 1982: Development of a turbulence closure model for geophysical fluid problems. *Rev. Geophys. Space Phys.*, **20**, 851–875.
- Miyahara, S., 1984: A numerical simulation of the zonal mean circulation of the middle atmosphere including effects of solar diurnal tidal waves and internal gravity waves-solstice conditions. *Dynamics of the Middle Atmosphere*, J. R. Holton and T. Matsuno, Eds., Terra, 271–287.
- Pepper, D. W., C. D. Keen, and J. P. E. Long, 1979: Modeling the dispersion of atmospheric pollution using cubic splines and cheapeau functions. *Atmos. Environ.*, **13**, 223–237.
- Roble, R. G., 1995: Energetics of the mesosphere and thermosphere. *The Upper Mesosphere and Lower Thermosphere: A Review of Experiment and Theory*, *Geophys. Monogr.*, No. 87, R. M. Johnson and T. L. Killeen, Eds., American Geophysical Union, 1–20.
- , and E. C. Ridley, 1994: A thermosphere-ionosphere-mesosphere-electrodynamics general circulation model (time-gcm): Equinox solar cycle minimum simulations (30–500 km). *Geophys. Res. Lett.*, **21**, 417–420.
- , —, and R. E. Dickinson, 1987: On the global mean structure of the thermosphere. *J. Geophys. Res.*, **92**, 8745–8758.
- Röttger, J., P. K. Rastogi, and R. F. Woodman, 1979: High-resolution vhf radar observations of turbulence structures in the mesosphere. *Geophys. Res. Lett.*, **6**, 617–620.
- Tapp, M. C., and P. W. White, 1976: A non-hydrostatic mesoscale model. *Quart. J. Roy. Meteor. Soc.*, **102**, 277–296.
- Tennekes, H., and J. L. Lumley, 1972: *A First Course in Turbulence*. The MIT Press, 300 pp.
- Theon, J. S., W. Nordberg, C. B. Katchen, and J. J. Horvath, 1967: Some observations on the thermal behavior of the mesosphere. *J. Atmos. Sci.*, **24**, 428–438.
- Walterscheid, R. L., and G. Schubert, 1990: Nonlinear evolution of an upward propagating gravity wave: Overtuning, convection, transience and turbulence. *J. Atmos. Sci.*, **47**, 101–125.
- Weinstock, J., 1976: Nonlinear theory of acoustic-gravity waves, 1. Saturation and enhanced diffusion. *J. Geophys. Res.*, **81**, 633–652.
- , 1982: Nonlinear theory of gravity waves, momentum deposition, generalized rayleigh friction, and diffusion. *J. Atmos. Sci.*, **39**, 1698–1710.
- Yamada, T., 1977: A numerical experiment on pollutant dispersion in a horizontally-homogeneous-atmospheric boundary layer. *Atmos. Environ.*, **11**, 1015–1024.
- , 1983: Simulations of nocturnal drainage flows by a $q^2 - l$ turbulence closure model. *J. Atmos. Sci.*, **40**, 91–106.
- , and G. L. Mellor, 1975: A simulation of the Wangara atmospheric boundary layer data. *J. Atmos. Sci.*, **32**, 2309–2329.